

Review

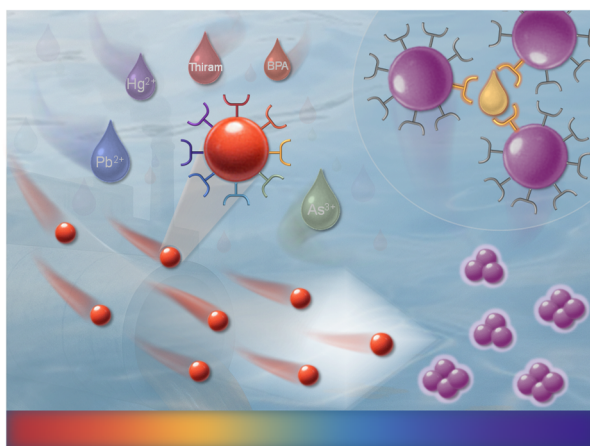
Colorimetric Plasmonic Nanosensors for Environmental Pollution Monitoring

Xueyong Zhang¹, Antonios G. Kanaras^{2,3}, and Yadong Yin^{1,*}¹ Department of Chemistry, University of California, Riverside, CA 92521, USA² Department of Chemistry, School of Science, National and Kapodistrian University of Athens, Zografou, 15772 Athens, Greece³ School of Physics and Astronomy, University of Southampton, Highfield, Southampton SO17 1BJ, UK

* Correspondence: yadong.yin@ucr.edu

Received: 7 April 2025; Revised: 9 June 2025; Accepted: 13 June 2025; Published: 9 July 2025

Abstract: Environmental pollution, particularly water contamination by heavy metals and organic pollutants, presents a critical global challenge requiring effective monitoring solutions. Colorimetric plasmonic nanosensors, primarily utilizing gold nanoparticles (AuNPs) due to their exceptional stability and tunable optical properties, offer a promising approach for rapid, cost-effective, and label-free pollutant detection. This review highlights recent advancements in AuNP-based colorimetric plasmonic nanosensors for environmental monitoring. We explore their fundamental sensing mechanisms and critically examine their applications in detecting a broad spectrum of waterborne contaminants, including heavy metals, inorganic species, and diverse organic pollutants. By showcasing the versatility and potential of these emerging technologies, this review emphasizes their significant contribution towards developing more efficient and accessible tools for mitigating environmental pollution and protecting public health.



Keywords: nanosensor; pollution; surface plasmon resonance; nanoparticle; plasmonic coupling; aggregation

1. Introduction

Environmental pollution has become a critical global crisis, driven by rapid industrialization, urbanization, and unsustainable human activities [1]. Among the most pressing concerns is water pollution, which affects billions of people worldwide [2]. Over 80% of sewage is discharged into rivers and oceans without proper treatment, leading to widespread environmental degradation and increased disease prevalence [2,3]. Heavy metal contamination, particularly from toxic elements such as lead (Pb), cadmium (Cd) and mercury (Hg), poses a severe threat due to their bioaccumulative nature, resulting in long-term toxicity and ecological disruptions [4]. Additionally, organic pollutants from wastewater discharge contribute to oxygen depletion in aquatic ecosystems, elevating biochemical oxygen demand levels and endangering marine and freshwater life [5,6]. These combined factors underscore the urgent need for effective pollution control strategies to safeguard public health and the environment.

Given the growing concerns over environmental pollution, developing advanced monitoring technologies is essential for effective detection and mitigation strategies. Traditional analytical techniques, including gas chromatography [7], mass spectrometry [8], atomic absorption and emission spectroscopy [9], and high-performance liquid chromatography [10], provide high sensitivity and precision but are hindered by high costs, complex sample preparation, specialized equipment, and lengthy processing times. Furthermore, they are unsuitable for rapid, on-site monitoring, which is vital for timely pollution control. To overcome these limitations, there is growing interest in cost-effective and rapid detection methods.



Copyright: © 2025 by the authors. This is an open access article under the terms and conditions of the Creative Commons Attribution (CC BY) license (<https://creativecommons.org/licenses/by/4.0/>).

Publisher's Note: Scilight stays neutral with regard to jurisdictional claims in published maps and institutional affiliations.

Colorimetric plasmonic nanosensors offer high sensitivity, rapid response, and real-time detection capabilities [11–13], representing a class of cost-effective, label-free, and highly tunable alternatives to conventional analytical techniques for monitoring environmental pollution. Their detection mechanism relies on localized surface plasmon resonance (LSPR), where plasmonic nanoparticles, such as gold and silver nanoparticles, exhibit measurable optical shifts in response to analyte-induced changes in interparticle distance, particle size, or surface chemistry. This property enables colorimetric detection, allowing pollutants to be identified visually or with simple optical devices, eliminating the need for sophisticated laboratory settings.

Gold nanoparticles (AuNPs) are the most popular building blocks for plasmonic nanosensors due to their high stability, biocompatibility, and highly tunable surface chemistry. While silver and copper nanoparticles are also plasmonically active, they are susceptible to oxidation and degradation under environmental conditions. The high chemical stability of AuNPs ensures low toxicity and long-term sensor reliability [14]. In addition, their well-defined optical properties and ability to be functionalized with a wide range of ligands further enhance their selectivity and sensitivity toward specific pollutants. These characteristics make AuNPs particularly well-suited for the development of robust colorimetric nanosensors.

As pollution continues to pose a significant threat to ecosystems and public health, colorimetric plasmonic nanosensors offer a promising approach for rapid and accessible environmental monitoring. This review explores recent advancements in AuNP-based colorimetric plasmonic nanosensors for environmental pollution monitoring, with a specific focus on their applications in detecting heavy metals, inorganic contaminants, and a wide range of organic pollutants. By leveraging these emerging technologies, more efficient and accessible solutions can be developed to mitigate environmental pollution.

2. Fundamentals of Plasmonic Nanomaterials in Environmental Sensing

2.1. LSPR—The Basis of Colorimetric Sensing

LSPR is the fundamental principle behind colorimetric plasmonic sensors. It occurs when conduction electrons on the surface of plasmonic nanoparticles collectively oscillate in response to incident light (Figure 1A) [15]. The resonance frequency depends on several factors, including nanoparticle size, shape, interparticle distance, and the surrounding medium [16,17]. As shown in Figure 1B, for small spherical AuNPs, the primary extinction peak appears at 525 nm and progressively redshifts as the particle size increases. With larger particles, light scattering becomes more prominent, significantly influencing the overall optical properties [18]. In contrast to spherical AuNPs, gold nanorods (AuNRs) exhibit two distinct plasmonic peaks owing to their anisotropic shape: a transverse plasmon peak, which is associated with electron oscillation along the short axis, and a longitudinal plasmon peak, which occurs along the long axis. As the aspect ratio (length-to-width ratio) of AuNRs increases, the longitudinal plasmon peak redshifts significantly into the near-infrared (NIR) region, while the transverse plasmon peak remains relatively unchanged in the visible range (Figure 1C) [19]. This tunability in optical response makes AuNRs particularly useful for applications in biosensing, imaging, and photothermal therapy, where NIR light penetration is required [20,21].

Plasmonic coupling in LSPR-based sensing occurs when nanoparticles come into close proximity, leading to strong plasmonic interactions. In a well-dispersed state, individual AuNPs exhibit a distinct LSPR peak in the visible spectrum, typically producing a red-colored solution, as shown in Figure 1B. As illustrated in the electrodynamic modeling in Figure 1D, the plasmon band redshift becomes increasingly pronounced as the distance between the AuNP dimer decreases [22]. When this distance becomes smaller than the nanoparticle diameter, plasmon coupling becomes significant, resulting in a redshift of the LSPR peak due to the formation of lower-energy collective plasmonic modes [23]. Experimental results confirm this redshift, accompanied by a visible color change from red to purple (Figure 1E) [24]. The resulting spectral redshift and broadening form the basis of most aggregation-based colorimetric sensors.

2.2. Mechanisms of Colorimetric Responses in Plasmonic Sensors

The ability of AuNP-based colorimetric sensors to detect analytes relies on distinct plasmonic modulation mechanisms that induce measurable optical shifts. The most common mechanism is aggregation-based sensing, where AuNPs undergo a red-to-blue/purple color change due to interparticle plasmonic coupling when they come into proximity. In contrast, anti-aggregation mechanisms prevent nanoparticle aggregation, preserving their dispersed state and maintaining the original red color even under conditions that would otherwise promote aggregation, such as the presence of salt or interfering species. Other mechanisms, such as etching-based sensing, involve oxidative dissolution of AuNRs, causing a color fade or blue shift due to a reduction in particle size, while

growth-based sensing results in nanoparticle enlargement, shifting the LSPR peak toward longer wavelengths and intensifying the red color.

Among these, aggregation-based sensing is the most widely used due to its simplicity and strong optical response. Aggregation can be triggered through several different pathways, including crosslinking-induced aggregation, destabilization-induced aggregation, and competitive binding-induced aggregation.

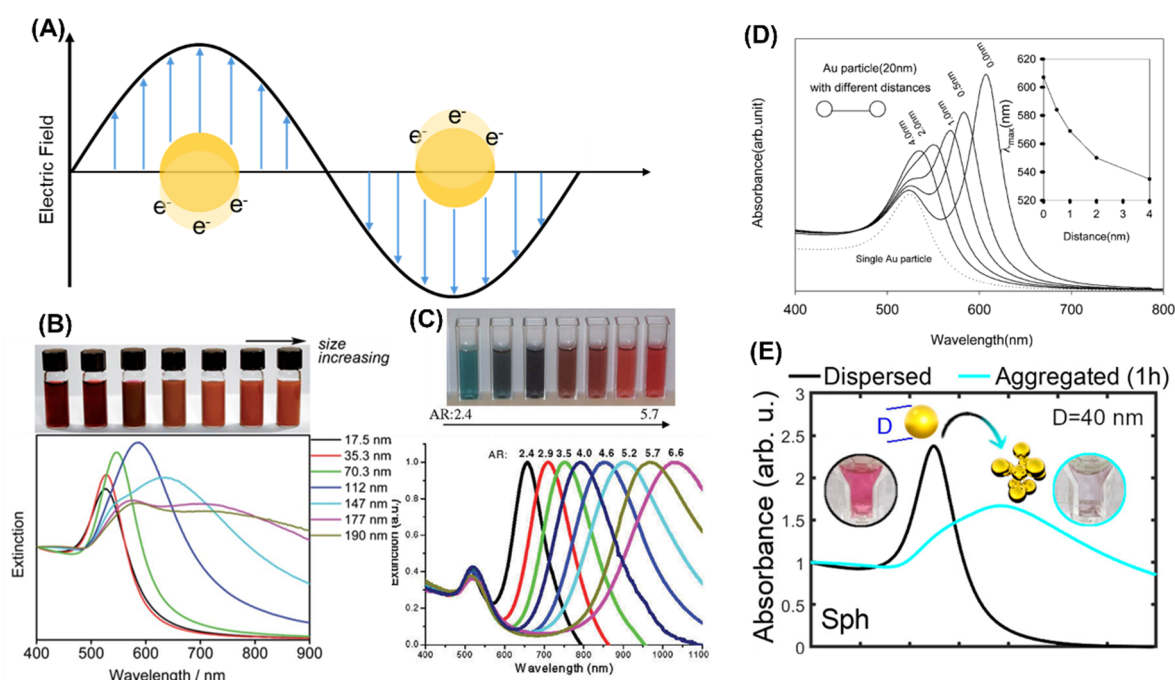


Figure 1. LSPR Principles and Spectral Shifts: Effects of Particle Size, Shape, and Aggregation in Au Nanostructures (A) Scheme of LSPR. (B) Photographic images and corresponding UV–Vis–NIR spectra of colloidal AuNPs with different particle sizes. Reproduced with permission [18]. Copyright 2012, Royal Society of Chemistry. (C) Photographic images and corresponding UV–Vis–NIR spectra of colloidal AuNRs with different aspect ratios. Reproduced with permission [19]. Copyright 2010, University of Cairo. (D) Electrodynamic simulations of 20 nm AuNP showing extinction spectra at varying interparticle distances, with the inset illustrating the corresponding plasmon peak shift as a function of spacing. Reproduced with permission [22]. Copyright 2004, American Chemical Society. (E) Typical spectral shift observed in colloidal sensors based on the aggregation of spherical nanoparticles with diameter D. Reproduced with permission [24]. Copyright 2023, American Chemical Society.

2.3. Aggregation-Based Colorimetric Sensing

Aggregation-induced plasmonic coupling significantly alters the optical properties of AuNPs, making this approach highly effective for colorimetric sensing. One common mechanism is crosslinking-induced aggregation, where the analyte acts as a crosslinker, binding multiple nanoparticles together. This typically occurs when the analyte has multiple binding sites that interact with AuNP surfaces, leading to the formation of large aggregates (Figure 2A). Examples include metal ions such as Pb^{2+} and Hg^{2+} , which can bridge AuNPs via specific interactions, causing a distinct red-to-blue color shift [25,26].

Another widely used mechanism is destabilization-induced aggregation, where the analyte disrupts the stabilizing ligands on the nanoparticle surface, reducing electrostatic repulsion and allowing AuNPs to aggregate. This can occur through charge screening, such as in salt-induced aggregation, where high ionic strength neutralizes the surface charge on AuNPs, leading to uncontrolled aggregation (Figure 2B). Similarly, cationic analytes like As^{3+} and Hg^{2+} can bind with the specific designed aptamers on AuNP surfaces, triggering aggregation and a corresponding color change [27,28].

Competitive binding-induced aggregation occurs when the analyte competes with existing stabilizing molecules on the AuNP surface, displacing them and promoting aggregation (Figure 2C). For example, thiol-containing molecules can replace citrate ligands on AuNPs, leading to ligand exchange and subsequent aggregation [29].

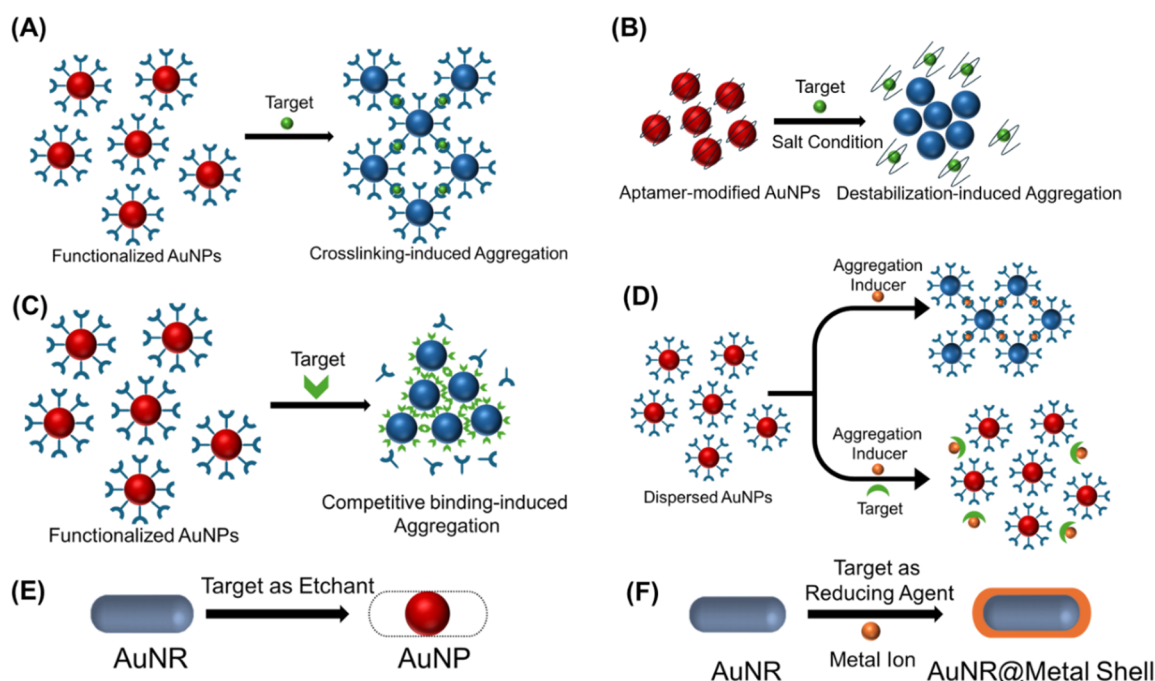


Figure 2. Mechanisms of Colorimetric Responses in Plasmonic Sensors. (A) Scheme for crosslinking-induced aggregation. (B) Scheme for destabilization-induced aggregation. (C) Scheme for Competitive binding -induced aggregation. (D) Scheme for anti-aggregation-based sensing. (E) Scheme for etching-based sensing. (F) Scheme for growth-based sensing.

2.4. Other Colorimetric Mechanisms: Anti-Aggregation, Etching and Growth

While aggregation-based sensing is the dominant strategy, other plasmonic mechanisms also contribute to colorimetric detection. Anti-aggregation-based sensing operates in the opposite manner to aggregation; here, the analyte prevents AuNPs from aggregating by stabilizing their dispersed state (Figure 2D). For example, Pb^{2+} can induce DNA strand cleavage, releasing a fragment that adsorbs onto the AuNP surface, thereby stabilizing the nanoparticles and preventing aggregation under high-salt conditions [30].

Etching-based sensing involves the oxidative dissolution of AuNPs, leading to a reduction in particle size and a corresponding shift in LSPR (Figure 2E). For example, nitrite (NO_2^-) can etch AuNRs to soluble Au species, resulting in the fading or disappearance of the original color [31].

Growth-based sensing involves the deposition of additional material onto existing AuNPs in the presence of a reducing agent, resulting in a plasmonic peak shift and a visible color change (Figure 2F). A common example is the reduction of Ag^+ by formaldehyde, which leads to silver shell growth on AuNRs and alters their optical properties, producing noticeable shifts in color depending on the extent of silver deposition [32].

2.5. Surface Functionalization of AuNPs for Colorimetric Sensing

The functionalization of AuNPs plays a crucial role in enhancing their selectivity and stability for colorimetric sensing applications. The most commonly used AuNPs are citrate-stabilized, relying on electrostatic repulsion between negatively charged citrate ligands to maintain colloidal stability [33]. However, citrate-capped AuNPs often lack sufficient selectivity [34] and sensitivity [25], prompting the need for further surface modification with specific ligands that interact selectively with target analytes. Among various strategies, thiol-based functionalization is widely employed, as thiol groups form strong Au–S bonds, enabling stable attachment of molecules such as glutathione (GSH) [35–37] and cysteine [38]. These ligands not only enhance selectivity but also improve nanoparticle stability under diverse conditions. Amine-functionalized AuNPs offer another approach, where amino groups interact with the Au surface, as seen in melamine-modified systems [39].

A highly effective strategy for achieving selective detection involves incorporating both a recognition element and a thiol group into the same molecule—allowing it to react with the target analyte while anchoring firmly onto the AuNP surface. This dual-binding design ensures both analyte recognition and nanoparticle stability, minimizing nonspecific aggregation. For instance, thiolated thymine can selectively bind Hg^{2+} [26], thiolated crown ethers target specific metal ions [40], and thiolated DNA is commonly used for specific recognition [41,42].

Tailoring the surface chemistry of AuNPs makes it possible to significantly enhance sensor performance, enabling sensitive and selective detection of a wide range of pollutants, biomolecules, and metal ions.

2.6. Synthesis of AuNPs for Colorimetric Sensing Applications

In colorimetric sensing, the Turkevich method is the most widely adopted for synthesizing AuNPs, producing citrate-stabilized AuNPs by reducing HAuCl₄ with trisodium citrate in boiling water [43]. These nanoparticles are widely adopted due to their simple synthesis and ease of post-synthetic functionalization. Molecules such as GSH [35], melamine [39], and aptamers [44] can readily replace the citrate ligands, enabling the introduction of selective recognition elements while maintaining colloidal stability for sensing applications. In addition to this classical approach, green synthesis methods—using reducing agents such as tannic acid [45] and gallic acid [46]—have been proposed for their environmental friendliness and biocompatibility.

AuNRs are also valuable tools for investigating etching processes and growth mechanisms. A typical seed-mediated synthesis of short AuNRs involves hexadecyltrimethylammonium bromide (CTAB), silver nitrate, and ascorbic acid. In this method, silver ions are essential for directing rod formation and minimizing spherical byproducts, with aspect ratios finely controlled through the seed-to-metal precursor ratio and reagent concentrations [47]. Building on this, the incorporation of aromatic additives into the CTAB-based system enables AuNR synthesis under reduced CTAB concentrations, while significantly enhancing monodispersity and tunability [48].

3. Detection of Inorganic Species

AuNP-based colorimetric sensing has been extensively applied to the detection of inorganic species, owing to its simplicity, high sensitivity, and visual readout. Reported systems include a wide range of analytes such as heavy metals (Pb²⁺, As³⁺, Hg²⁺, Tl⁺, Ag⁺), other metal ions (Sc³⁺, Cs⁺, Al³⁺), and anionic pollutants (CN⁻, NO₂⁻). In addition to single-target detection, several studies have demonstrated the simultaneous detection of multiple species using tailored surface ligands or differential response patterns, expanding the applicability of these sensors to complex environmental and biological samples.

3.1. Detection of Lead Species

Lead ion and other lead species are highly toxic, persistent, and bioaccumulative pollutants, primarily released from industrial activities, lead-based paints, batteries, and contaminated water sources [49,50]. Lead exposure poses severe health risks, particularly to the nervous system, kidneys, and cognitive development in children [51,52]. Given its environmental persistence and toxicity, effective monitoring of lead contamination is crucial for pollution control and public health protection.

Lu et al. have developed a series of DNAzyme-mediated AuNP sensors for Pb²⁺ detection, utilizing an anti-aggregation mechanism with distinct strategies [30,41,42]. In 2003, a Pb²⁺-specific DNAzyme was employed to regulate AuNP assembly through DNA hybridization. The system consisted of AuNPs functionalized with thiol-modified DNA strands (DNA_{Au}), where the thiol end binds to the AuNP surface, along with the DNAzyme and a DNA substrate (Sub_{Au}) that hybridizes specifically to both ends of DNA_{Au} while maintaining the DNAzyme recognition portion. The hybridization between DNA_{Au} and Sub_{Au} brought the AuNPs closer together, leading to aggregation and a blue color change. In the presence of Pb²⁺, the DNAzyme selectively cleaved the substrate strand, disrupting hybridization, preventing aggregation, and producing a red color (Figure 3A). However, this method required a two-hour heating and cooling cycle to facilitate hybridization [41]. To accelerate the process, in 2004, the design was improved by optimizing nanoparticle alignment and size, enabling faster detection in less than 10 min at room temperature [42]. Later, in 2008, Lu's group introduced a label-free sensor that eliminated the need for thiol-ended DNA to modify AuNPs and instead relied on the property of AuNPs aggregating in a high-ionic-strength environment. In this system, unmodified AuNPs and DNAzyme complex were treated under high-salt conditions. In the presence of Pb²⁺, single-stranded DNA was released from the complex and adsorbed onto AuNPs, preventing their aggregation under high-salt conditions (Figure 3B). This approach simplified sensor fabrication, and lowered the detection limit to 3 nM, surpassing regulatory standards. Additionally, pH-controlled tunability was introduced, allowing for the adjustment of the detection range for different environmental applications [30].

The synthesis of DNA oligomers can be complex and expensive, highlighting the need for a simple and cost-effective colorimetric sensor for Pb²⁺ detection. One alternative approach relies on the aggregation mechanism, in which Pb²⁺ binds to functional groups on AuNPs, triggering their aggregation and causing a red-to-blue color shift. Frost et al. investigated the interaction between citrate-capped AuNPs and divalent heavy metal ions (Pb²⁺, Cd²⁺, Ni²⁺, and Hg²⁺), elucidating the molecular interactions responsible for Pb²⁺-induced aggregation. ATR-FTIR and computational simulations showed that Pb²⁺ uniquely binds to both unbound carboxylate groups of citrate,

effectively neutralizing the negative charge stabilizing AuNPs. In contrast, Cd^{2+} , Ni^{2+} , and Hg^{2+} primarily interact with already-bound carboxylate groups or exhibit weaker binding, failing to fully neutralize the surface charge. This charge neutralization by Pb^{2+} was further supported by zeta potential and pH measurements, which demonstrated a reduction in AuNP surface charge from -44.3 mV to nearly neutral (-1.1 mV), leading to a significant loss of electrostatic repulsion and rapid aggregation. Additionally, Pb^{2+} caused a major pH drop (from 6.3 to 1.0), further altering surface chemistry and reinforcing nanoparticle destabilization [53]. A basic citrate-capped AuNP sensor exploits this mechanism, detecting Pb^{2+} via direct complexation with carboxyl groups, achieving a detection limit of $18 \mu\text{M}$ [25].

GSH-functionalized AuNPs (GSH-AuNPs) have been widely used for Pb^{2+} detection as a more sensitive alternative to citrate-capped AuNPs [35,36]. In this system, thiol groups in glutathione strongly bind to the AuNP surface, while carboxyl and amino groups remain available for metal ion coordination. To minimize interference from other metal ions, the amino group is protonated to ammonium by adjusting the pH to 8, ensuring that only the carboxyl groups participate in Pb^{2+} binding. This enhances Pb^{2+} selectivity and allows it to induce aggregation in a manner similar to citrate-capped AuNPs but with improved sensitivity (Figure 3C). GSH-AuNPs in the presence of salt have been successfully used to detect Pb^{2+} with a detection limit of 100 nM [35]. The aggregation of AuNPs leads to an increase in particle size, which can be more effectively detected using dynamic light scattering (DLS). By tracking these size changes, DLS-enhanced detection achieves an ultrasensitive limit of 100 ppt, making it suitable for analyzing Pb^{2+} in water, plastic toys, and paint [36].

Biocompatible materials such as tannic acid and gallic acid have been explored for AuNP functionalization [45,46,54]. Gallic acid stabilizes AuNPs through carboxylate interactions, while Pb^{2+} binds primarily to phenolic groups, inducing aggregation. The limit of detection (LOD) for Pb^{2+} using gallic acid-functionalized AuNPs is reported at the micromolar level [46]. Narrowing the size distribution and optimizing pH further reduced the LOD to 10 nM [54]. Another polyphenolic compound, tannic acid, has also been used to stabilize AuNPs, achieving an LOD of 60 ng/mL ($0.29 \mu\text{M}$) [45]. An alternative approach involves triazole-acetate-functionalized AuNPs, where a dithiol group facilitates attachment to the AuNP surface. Pb^{2+} binds to both carboxyl groups and the triazole ring, forming a stronger and more selective coordination complex (Figure 3D). This mechanism enhances selectivity over other metal ions and enables a lower detection limit of 16.7 nM [55].

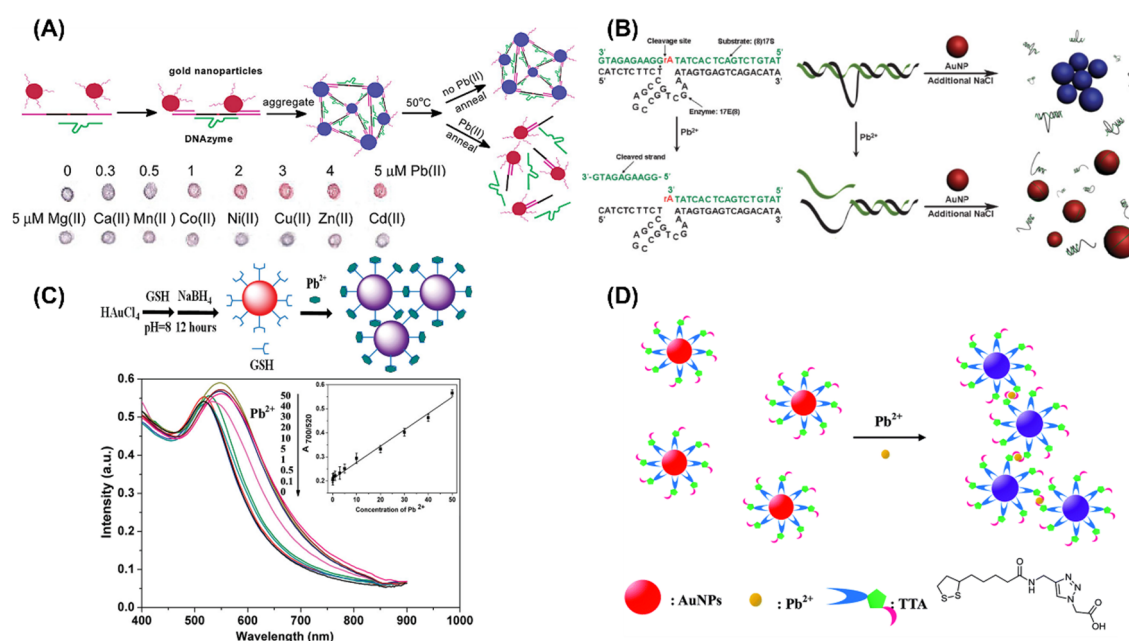


Figure 3. Colorimetric sensing strategies for Pb^{2+} detection using AuNP-based sensors. (A) Schematic of an anti-aggregation mechanism for Pb^{2+} detection, along with the visible color response on an alumina TLC plate at varying Pb^{2+} concentrations and in the presence of other divalent metal ions. Reproduced with permission [41]. Copyright 2003, American Chemical Society. (B) Anti-aggregation-based, label-free colorimetric sensing of Pb^{2+} . Reproduced with permission [30]. Copyright 2008, Wiley. (C) Detection of Pb^{2+} using GSH-AuNPs. Top: Schematic illustration of the sensing mechanism. Bottom: UV-vis absorption spectra of GSH-AuNPs after the addition of Pb^{2+} of varying concentrations. Reproduced with permission [35]. Copyright 2010, American Chemical Society. (D) Pb^{2+} detection via triazole-acetate-functionalized AuNPs. Reproduced with permission [55]. Copyright 2014, Royal Society of Chemistry.

3.2. Detection of Arsenic Species

Arsenic is a highly toxic metalloid, with its inorganic forms (As^{3+} and As^{5+}) posing the greatest hazard. As a persistent environmental pollutant, arsenic contaminates groundwater through natural geology, mining, and industrial discharge, making it a widespread concern [56]. Long-term exposure to arsenic-contaminated water leads to severe health effects, including skin lesions, peripheral neuropathy, organ damage, and an increased risk of cancer [57].

As^{3+} , like Pb^{2+} , can be detected through AuNP aggregation mechanisms, where its interaction with surface ligands triggers nanoparticle clustering and a visible red-to-blue color change. Citrate-capped AuNPs can also be used for As^{3+} detection, with As^{3+} binding to carboxyl groups to induce aggregation. Interestingly, as-synthesized citrate-capped AuNPs are not initially sensitive to As^{3+} . However, after removing excess citrate via dialysis, the detection limit improves significantly to 1.8 ppb (Figure 4A). When evaluating the selectivity of dialyzed citrate-capped AuNPs, 256 ppb (1.24 μM) of various metal ions, including Pb^{2+} , did not induce a color change [58]. However, it has been reported that Pb^{2+} requires a concentration of 18 μM to cause aggregation [25]. This suggests that while As^{3+} induces aggregation at much lower concentrations than Pb^{2+} , selectivity may become a concern at higher Pb^{2+} concentrations. Glucose, a biodegradable and biocompatible molecule, has also been used to functionalize AuNPs. It utilizes hydroxyl groups, achieving a detection limit of 0.53 ppb, with selectivity tests confirming no aggregation in the presence of Pb^{2+} , Co^{2+} , Hg^{2+} , Cd^{2+} , Ni^{2+} , or Cu^{2+} [59]. Similarly, GSH-AuNPs rely on carboxyl groups, detecting As^{3+} down to 0.12 ppb via RGB-based image quantification. However, Pb^{2+} also induces weak aggregation, indicating partial selectivity [37].

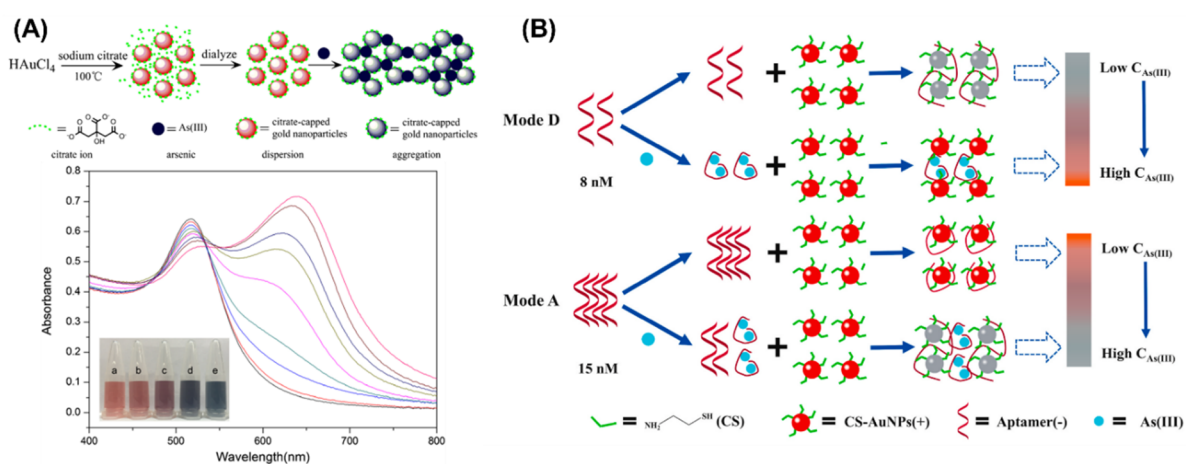


Figure 4. Colorimetric sensing strategies for As^{3+} detection using AuNP-based sensors. (A) Top: Schematic illustration of As^{3+} detection via dialyzed citrate-capped AuNPs. Bottom: UV-vis absorption spectra of citrate-AuNPs after the addition of As^{3+} of varying concentrations. Reproduced with permission [58]. Copyright 2017, Springer. (B) Bimodal detection of As^{3+} based on electrostatic attraction between positively charged AuNPs and a negatively charged As^{3+} aptamer, enabling both direct (Mode D) and amplified (Mode A) sensing modes. Reproduced with permission [27]. Copyright 2022, Elsevier.

Multifunctional groups enhance arsenic detection by providing strong binding sites for both AuNP attachment and metal coordination. GSH forms Au-S bonds via its thiol group, while its carboxyl and amino groups facilitate metal ion binding. Dithiothreitol (DTT) stabilizes AuNPs through Au-S bonds and reduces As (V) to As (III), making both oxidation states detectable. Cysteine (Cys), a thiol and amine containing amino acid, interacts with both AuNPs and metal ions, reinforcing the detection mechanism. 2,6-Pyridinedicarboxylic acid (PDCA) selectively binds to As^{3+} , further improving specificity. The GSH-DTT-Cys-PDCA functionalized AuNPs achieve a detection limit of 2.5 ppb, making them highly sensitive for arsenic detection [38].

The highest selectivity is achieved with a dual-mode aptamer-based sensor, where an As^{3+} -specific aptamer regulates nanoparticle aggregation and re-dispersion, minimizing false positives. The mechanism relies on electrostatic interactions between negatively charged aptamers and positively charged AuNPs. At low aptamer concentrations (Mode D, 8 nM), aptamers cross-link AuNPs, inducing aggregation and a red-to-blue shift. As^{3+} binding sequesters aptamers, breaking cross-links and re-dispersing AuNPs (blue-to-red shift). Conversely, at high aptamer concentrations (Mode A, 15 nM), aptamers fully coat AuNPs, preventing aggregation. As^{3+} binding removes aptamers, destabilizing AuNPs and triggering aggregation (Figure 4B). This dual-mode system enhances specificity, achieving LOD values of 0.41 ppb (Mode A) and 0.57 ppb (Mode D) for As^{3+} detection [27].

3.3. Detection of Mercury Species

Mercury is a persistent environmental pollutant released from industrial activities, coal combustion, and mining, accumulating in water bodies and soil [60]. Its highly toxic forms, particularly methylmercury, bioaccumulate in the food chain, posing serious risks to ecosystems and human health [61].

Hg^{2+} can be detected using AuNP-based colorimetric sensors through different mechanisms, primarily relying on thymine- Hg^{2+} -thymine (T- Hg^{2+} -T) coordination chemistry. One straightforward approach is to functionalize thymine with a thiol group, allowing it to attach to AuNPs via Au-S bonds. Upon Hg^{2+} addition, T- Hg^{2+} -T coordination bridges the nanoparticles, inducing aggregation and a color change (Figure 5A). This method achieves a detection limit of 2.8 nM [26]. Alternatively, Hg^{2+} can be detected without thiolation by stabilizing AuNPs with ssDNA in a high-salt environment. When Hg^{2+} is introduced, T- Hg^{2+} -T coordination induces DNA hairpin formation, destabilizing the AuNPs and leading to aggregation in the presence of salt, with a LOD of 50 nM [28]. A further variation replaces salt with the cationic polymer poly(diallyldimethylammonium chloride) (PDDA) as the aggregation inducer. In the absence of Hg^{2+} , PDDA binds to negatively charged ssDNA, preventing AuNP aggregation. However, when Hg^{2+} is introduced, ssDNA folds into a hairpin structure, releasing free PDDA, which neutralizes the AuNP surface charge and triggers aggregation (Figure 5B). This approach offers ultrasensitive detection with a LOD of 0.15 nM [62]. Beyond T- Hg^{2+} -T interactions, another method employs diethyldithiocarbamate (DDTC) as a specific ligand for Hg^{2+} detection. In this approach, Cu^{2+} in the $\text{Cu}(\text{DDTC})_2$ complex is displaced by Hg^{2+} , releasing a thiol group that binds to AuNPs, leading to surface charge neutralization and aggregation. This method detects both Hg^{2+} (LOD: 10 nM) and methylmercury (LOD: 15 nM) [63]. In a different approach, Hg^{2+} can be detected through its direct interaction with AuNPs, forming Hg^{2+} -Au bonds that alter surface charge and stability. However, if citrate remains on AuNPs, it stabilizes them, making Hg^{2+} detection less effective. When citrate is removed, Hg^{2+} adsorption further reduces surface charge, promoting aggregation. This method is significantly less sensitive, with a LOD of 5 μM [64].

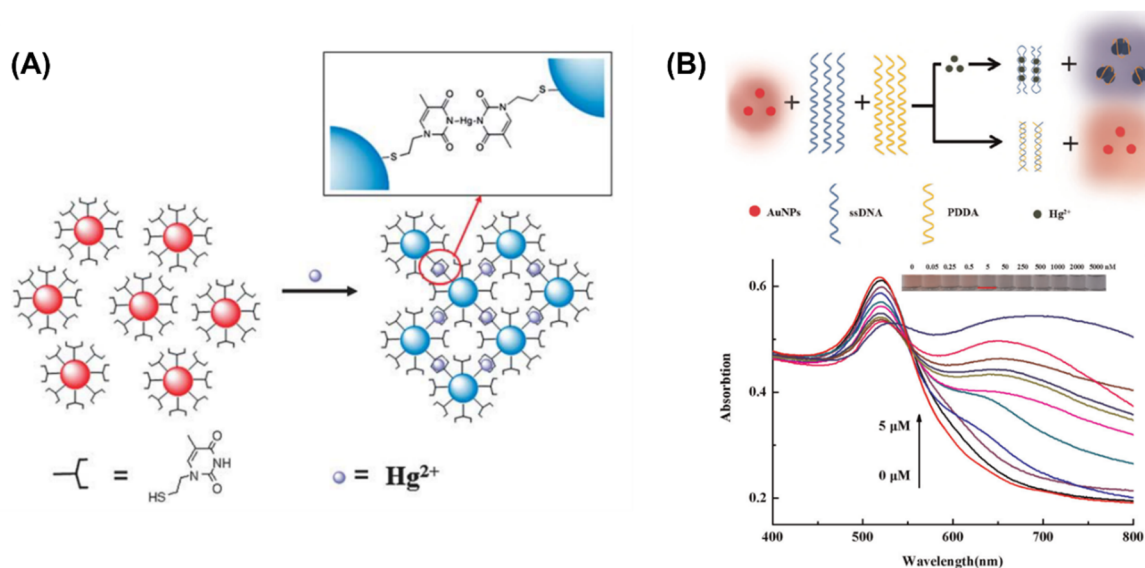


Figure 5. Colorimetric sensing strategies for Hg^{2+} detection using AuNP-based systems. (A) Schematic illustration of Hg^{2+} detection based on thymine- Hg^{2+} -thymine coordination chemistry. Reproduced with permission [26]. Copyright 2011, Royal Society of Chemistry. (B) Top: Detection mechanism of Hg^{2+} through AuNP aggregation modulated by PDDA, leveraging the specific binding between Hg^{2+} and ssDNA, along with electrostatic interactions between PDDA and ssDNA. Bottom: UV-vis absorption spectra of AuNPs after the addition of Hg^{2+} of varying concentrations. Reproduced with permission [62]. Copyright 2015, Elsevier.

3.4. Detection of Aluminum Species

Aluminum is a widespread environmental pollutant, primarily released through industrial activities, mining, and acid rain-induced leaching from soil into water sources [65]. Elevated aluminum levels in water and soil can be toxic to aquatic life, plants, and humans, and have been associated with neurodegenerative disorders, including Alzheimer's disease [66].

Citrate-capped AuNPs have also been used for Al^{3+} detection at an optimal pH of 2.9, achieving an LOD of 1.0 μM through Al^{3+} complexation with citrate ligands, which induces aggregation (Figure 6A). The pH was tuned

to eliminate interference from Fe^{3+} , while Pb^{2+} also triggered aggregation but with a longer response time. In contrast, Al^{3+} induced an immediate color change, making it more distinguishable. However, interference from Sb^{3+} and Cr^{3+} remained a challenge [34].

Beyond citrate-based detection, Al^{3+} coordination with hydroxyl groups has also been widely utilized in AuNP-based sensors. AuNPs have been functionalized with catechol ligands, including pyrocatechol, 3-(3,4-dihydroxyphenyl)propionic acid, dopamine, and levodopa, which strongly chelate with Al^{3+} . Upon Al^{3+} binding, these ligands dissociate from the AuNP surface due to their stronger affinity for Al^{3+} , leading to nanoparticle destabilization and aggregation. Among these, dopamine-functionalized AuNPs exhibited the highest sensitivity, achieving a LOD of $0.81 \mu\text{M}$ [67]. Similarly, N-lauroyltyramine has been used as a capping ligand, where Al^{3+} forms coordination complexes with hydroxyl groups, inducing AuNP aggregation with a detection limit of $1.15 \mu\text{M}$ [68]. Another approach employs Schiff base-functionalized AuNPs using N-(2-hydroxynaphthylidene)-2-aminoethanethiol (HNAET) as a chelating ligand for selective Al^{3+} detection (Figure 6B). The thiol group anchors HNAET to the AuNP surface, while the hydroxyl and imine groups strongly chelate Al^{3+} , achieving a detection limit of $0.29 \mu\text{M}$ [69].

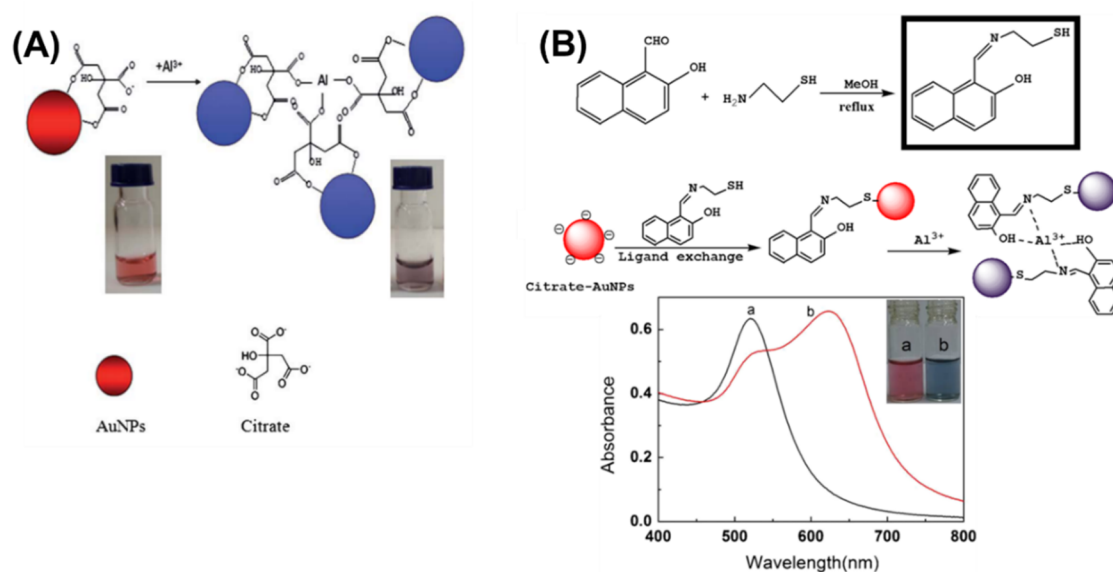


Figure 6. Colorimetric sensing strategies for Al^{3+} detection using AuNP-based sensors. (A) Schematic illustration of Al^{3+} sensing based on citrate-capped AuNPs. Reproduced with permission [34]. Copyright 2012, Royal Society of Chemistry. (B) Top: Synthesis of HNAET and the ligand exchange of HNAET onto AuNP surfaces and the corresponding signaling mechanism for Al^{3+} detection using the HNAET–AuNP probe. Bottom: UV–vis absorption spectra of citrate–AuNPs after the addition of Al^{3+} . Reproduced with permission [69]. Copyright 2016, Springer.

3.5. Detection of Cesium

Cesium primarily originates from nuclear accidents, industrial waste, and mining activities, posing environmental risks due to their long-term soil retention, and potential radiotoxicity [70].

Cs^+ can be detected using colorimetric sensors based on nonmorphological transitions of AuNPs. Cs^+ fits well into Prussian blue (PB) lattice and forms stable PB- Cs^+ complex. When Prussian blue precursor (PB-P) is added to the AuNP dispersion, citric acid reduces Fe^{3+} to Fe^{2+} , leading to the formation of a PB nanoshell on the AuNP surface, causing a color change from red to blue. However, in the presence of Cs^+ , PB-P preferentially reacts with Cs^+ . This interaction prevents PB deposition onto AuNPs, allowing them to retain their original red color (Figure 7A). The method achieved a naked-eye detection limit of $30 \mu\text{M}$ and a UV-Vis detection limit of $19 \mu\text{M}$ [71].

3.6. Detection of Silver Species

Silver pollution arises from industrial discharge, mining, and medical waste, with excessive levels causing toxicity in aquatic ecosystems and disrupting microbial communities [72].

A three-step aggregation–dispersion–reaggregation mechanism can be utilized for Ag^+ detection. First, AuNPs aggregate in the presence of quantum carbon dots, exhibiting a blue color. Then, upon addition of GSH, AuNPs redisperse, restoring the original red color. Finally, when Ag^+ ions are introduced, they preferentially bind

GSH, preventing AuNP redispersion and maintaining the aggregated state (Figure 7B). This method achieves detection limits of 50 nM (UV-Vis) and 140 nM (naked-eye) [73].

3.7. Detection of Thallium Species

Thallium pollution mainly originates from mining, smelting, and industrial waste, posing severe environmental and health risks due to its high toxicity, bioaccumulation, and adverse effects on the nervous [74].

A similar three-step mechanism is employed for Tl^+ detection. Initially, positively charged thioflavin T (ThT) induces AuNP aggregation. Subsequently, the addition of negatively charged PS2.M DNA displaces ThT, redispersing the AuNPs. Finally, when Tl^+ is introduced, DNA preferentially binds Tl^+ , releasing ThT, which reaggregates AuNPs (Figure 7C). This method demonstrates high selectivity and achieves a detection limit of 3.2 nM [75].

3.8. Detection of Scandium Species

Scandium, as a rare earth element, has been widely used in various industrial applications [76], leading to its extensive release into the environment through waste and emissions, which may pose risks to ecosystems and human health [77].

The three-step mechanism can also be adapted for Sc^{3+} detection. Initially, positively charged pyridoxal phosphate (PLP) aggregates negatively charged cysteamine-stabilized AuNPs. However, when Sc^{3+} is introduced, it strongly binds PLP, forming a stable complex that prevents PLP-induced aggregation, resulting in AuNP redispersion. This approach achieves high selectivity and a detection limit of 0.02 μM [78].

3.9. Detection of Cyanide

Cyanide pollution arises from industrial processes such as mining, electroplating, and chemical manufacturing, posing severe environmental and health risks due to its high toxicity, which can cause rapid aquatic life depletion [79] and human poisoning [80].

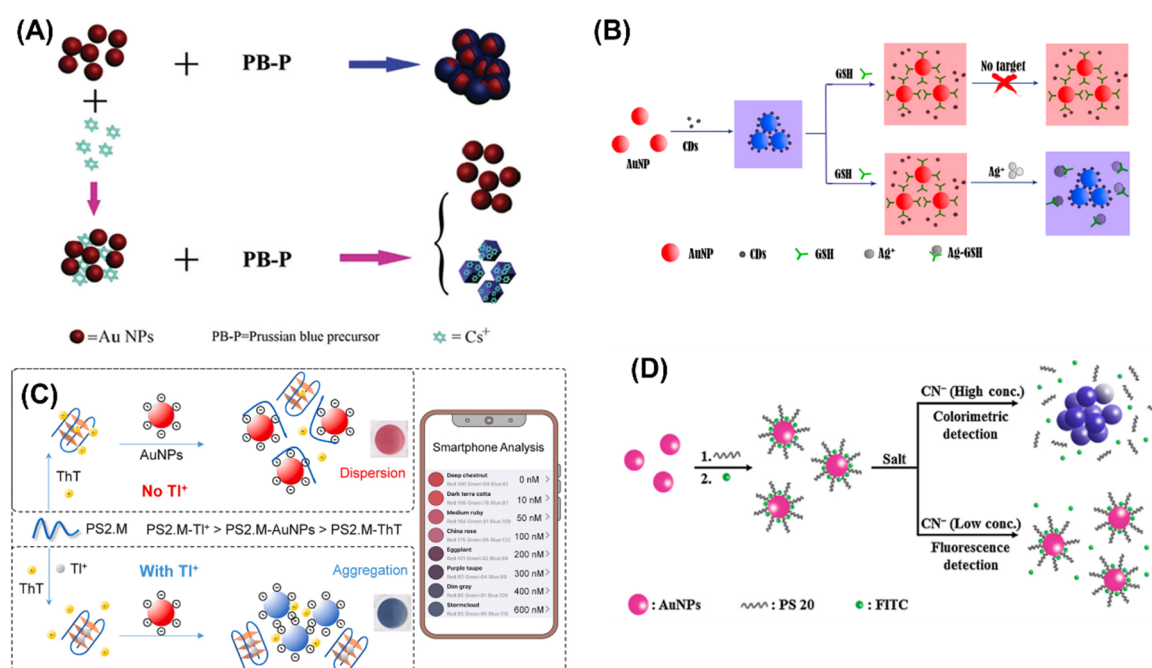


Figure 7. Colorimetric sensing strategies for Cs^+ , Ag^+ , Tl^+ , and CN^- detection using AuNP-based probes. (A) Sensing mechanism for Cs^+ detection based on the interaction between AuNPs and Prussian blue (PB). Reproduced with permission [71]. Copyright 2020, Royal Society of Chemistry. (B) Colorimetric detection of Ag^+ via stable AuNP aggregation triggered by carbon dots in the presence of GSH. Reproduced with permission [73]. Copyright 2018, American Chemical Society. (C) Thioflavin T-induced charge neutralization aggregation of AuNPs for Tl^+ detection. Reproduced with permission [75]. Copyright 2022, Elsevier. (D) Schematic illustration of the CN^- sensing mechanism based on the dual fluorescent and colorimetric response of AuNPs. Reproduced with permission [81]. Copyright 2016, Elsevier.

Cyanide can be detected by exploiting direct reactions with the AuNP surface, beyond traditional ligand-based aggregation mechanisms. In one approach, AuNPs stabilized by polysorbate 20 (PS20) and fluorescein isothiocyanate (FITC) have been employed to detect cyanide (CN⁻) through a surface-etching mechanism (Figure 7D). Initially, FITC fluorescence is quenched when attached to the AuNP surface. Upon CN⁻ addition, the AuNP surface is selectively etched, releasing FITC molecules into solution and restoring fluorescence intensity proportionally to the cyanide concentration (below 150 μM). At higher CN⁻ concentrations (>150 μM), extensive etching destabilizes the AuNPs beyond the protective capacity of PS20, leading to particle aggregation and a visible color shift from red to blue-gray, enabling naked-eye detection [81].

3.10. Detection of Nitrite

Nitrite is a harmful environmental pollutant commonly found in contaminated drinking water due to agricultural runoff and industrial waste [82]. It poses significant health risks, including methemoglobinemia and increased cancer risk, making its rapid and sensitive detection essential for water quality monitoring [83].

A highly sensitive and selective colorimetric sensor for NO₂⁻ was developed based on the etching of AuNRs, producing a visible color change from bluish green to red and eventually to colorless as NO₂⁻ concentration increases. Under acidic conditions, NO₂⁻ oxidizes Au to soluble species, causing preferential axial etching, which reduces the nanorod aspect ratio and induces a blue-shift in the longitudinal plasmon peak. CTAB enhances this process by stabilizing intermediate Au–Br or Au–Cl complexes. The sensor shows excellent selectivity and a detection limit of 0.5 μM and visible response at 4 μM, this system enables naked-eye detection and is promising for field applications [31].

3.11. Simultaneous Detection

While many colorimetric sensors are designed for the selective detection of a single metal ion, some approaches leverage broader interactions to enable the detection of multiple metal species.

Colorimetric sensor arrays provide effective platforms for simultaneously detecting and differentiating multiple metal ions. One array utilizes AuNPs functionalized with 11-mercaptoundecanoic acid combined with various amino acids (lysine, cysteine, histidine, tyrosine, and arginine) to detect Hg²⁺, Cd²⁺, Fe³⁺, Pb²⁺, Al³⁺, Cu²⁺, and Cr³⁺. The metal–ligand interactions produce distinct responses: some ions directly induce aggregation, some modulate aggregation cooperatively with amino acids, and others form stable metal–amino acid complexes, preventing aggregation (Figure 8A). This results in unique colorimetric fingerprints, enabling simultaneous detection and differentiation of these metal ions, with detection limits in the micromolar range (approximately 2–50 μM) [84]. Another array employs AuNPs individually functionalized with cysteine, glutathione, or melamine to discriminate among Ti⁴⁺, Cr³⁺, Mn²⁺, Fe³⁺, Pb²⁺, and Sn⁴⁺. Each metal ion produces a distinct colorimetric fingerprint, enabling accurate differentiation and quantification through linear discriminant analysis (LDA) with high selectivity and sensitivity in the concentration range of 100–900 nM [85].

Crown ether cavities can selectively bind metal ions such as Ba²⁺, Cd²⁺, and Pb²⁺. To attach crown ether (4'-aminobenzo-18-crown-6) onto AuNP surfaces, a thiol group is introduced via reaction with 3-mercaptopicnic acid, forming stable Au–S bonds. Metal ions (Ba²⁺, Cd²⁺, and Pb²⁺) interact selectively with the crown ether cavity, reducing electrostatic repulsion between AuNPs and inducing aggregation, resulting in a visible color shift (Figure 8B). Although this sensor achieves low detection limits (20 nM for Ba²⁺ and Cd²⁺; 50 nM for Pb²⁺), it cannot individually differentiate among these three ions, despite good selectivity over other tested metal ions [86]. Another approach employs thiolated calixarene ligands attached to AuNP surfaces, providing both aggregation-based and alloy-formation-based sensing mechanisms. In this method, Pb²⁺ ions cause AuNP aggregation by bridging nanoparticles through calixarene cavities, while Cu²⁺ ions undergo reduction upon interaction with AuNPs, forming an Au–Cu alloy shell via anti-galvanic exchange. This method achieves detection limits of 0.65 ppm for Cu²⁺ and 10 ppm for Pb²⁺ [40].

The binding between heavy metal ions and protein can also be utilized for sensing. Papain protein adsorbed on AuNPs via hydrophobic and electrostatic interactions. Metal ions bind specifically to the sulfur groups of papain's cysteine residues, reducing electrostatic repulsion and causing AuNP aggregation. This aggregation induces a visible color shift from red to blue, allowing easy, naked-eye detection. Although the sensor does not distinctly differentiate among Hg²⁺, Pb²⁺, and Cu²⁺ ions, it effectively discriminates them as a group from other common metal ions, with detection limits around 200 nM [87].

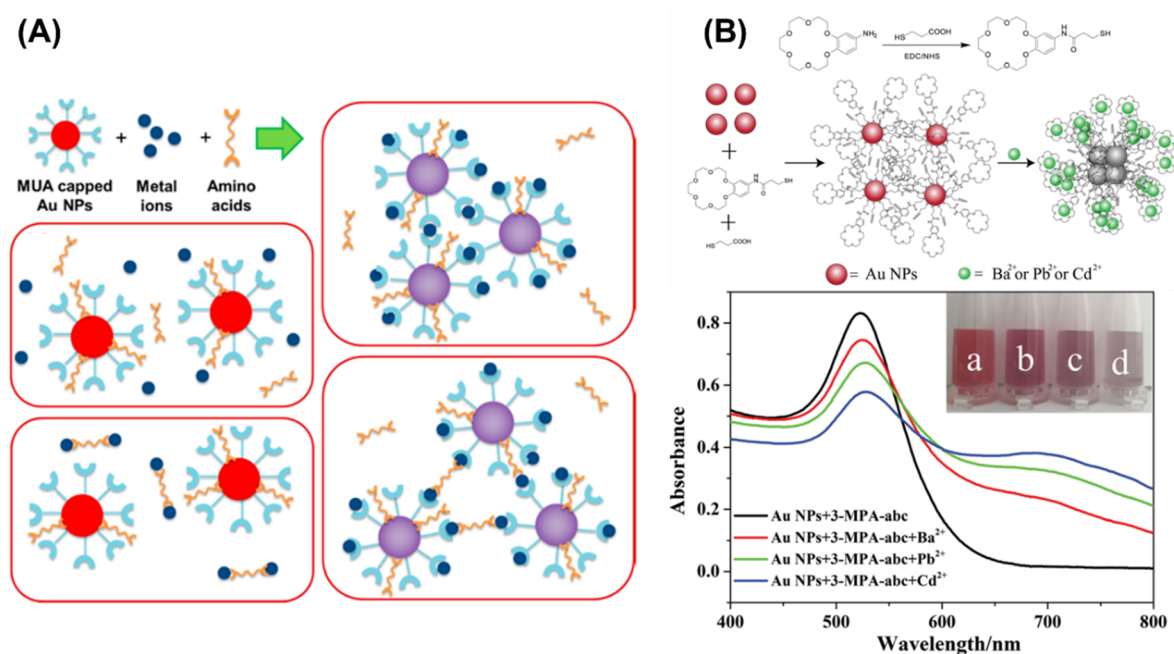


Figure 8. Simultaneous colorimetric detection of toxic metal ions using AuNP-based systems. (A) Schematic representation of the interactions among metal ions, amino acids, and AuNPs. Reproduced with permission [84]. Copyright 2014, American Chemical Society. (B) Top: Colorimetric detection mechanism of Ba²⁺, Pb²⁺, and Cd²⁺ using crown ether-functionalized AuNPs. Bottom: UV-vis absorption spectra crown ether-AuNPs after the addition of Ba²⁺, Pb²⁺, and Cd²⁺. Reproduced with permission [86]. Copyright 2019, Royal Society of Chemistry.

4. Detection of Organic Molecules

AuNP-based colorimetric sensing has been successfully applied to the detection of organic molecules. Reported systems include a wide variety of targets such as pesticides, fungicides, antibiotics, as well as food and environmental contaminants like clenbuterol, azodicarbonamide, bisphenol A (BPA), formaldehyde, T-2 toxin, and microcystin-LR.

4.1. Detection of Pesticides and Fungicide

Pesticides and fungicides are widely used in agriculture to protect crops from pests and diseases, but their environmental impact is a growing concern. These chemicals can leach into soil and water sources, leading to contamination that affects non-target organisms, including beneficial insects, aquatic life, and soil microbiota [88,89]. Many pesticides persist in the environment, accumulating in the food chain and posing long-term ecological and health risks. Excessive exposure to certain pesticides has been linked to neurological disorders, endocrine disruption, and cancer in humans [90].

A colorimetric sensor array utilizing citrate-capped AuNPs enables the discrimination of organophosphate pesticides (OPs) through their pH- and ionic strength-dependent interactions with citrate ligands (Figure 9A). OPs induce AuNP aggregation via hydrogen bonding and electrostatic interactions, with their affinity for citrate modulated by protonation or hydrolysis under varying pH conditions (4.5, 6.5, 9.0). Additionally, increasing ionic strength (0, 5, 15 mM NaCl) weakens citrate stabilization, altering aggregation behavior and generating distinct spectral response patterns for classification via hierarchical cluster analysis and LDA, with a detection range of 120–400 ng/mL [91]. A ligand exchange-based mechanism offers an alternative approach for pesticide discrimination, where pesticides containing thiol, amine, carbonyl, or nitrile functional groups replace citrate on AuNP surfaces, leading to destabilization, aggregation, and a red-to-blue color shift. Detection is pH-dependent, with acephate (346 nM), phenthoate (3.0 nM), and profenofos (600 nM) aggregating at pH 4; acetamiprid (0.624 nM) and chlorothalonil (375 nM) at pH 6; and cartap (17 nM) at neutral pH, demonstrating high selectivity and applicability in water and food analysis [29]. Citrate-capped AuNPs have also been used to detect terbutylazine (TBA) and dimethoate (DMT) via distinct charge-based mechanisms. TBA, carrying a strong positive charge, neutralizes citrate's negative charge, inducing aggregation and a red-to-blue color change. In contrast, DMT undergoes alkaline hydrolysis, producing negatively charged species that stabilize AuNPs, preventing aggregation and resulting in a gray-to-red color shift (Figure 9B). This sensor exhibited high selectivity, with LODs of 0.3 μM (visual) and 0.02 μM (UV-Vis) for TBA and 20 nM (visual) and 6.2 nM (UV-Vis) for DMT [92].

A label-free colorimetric assay has been developed for the detection of prothioconazole. The thiocarbonyl group in prothioconazole binds to AuNPs via Au–S interactions, while hydrogen bonding between prothioconazole molecules induces nanoparticle aggregation, resulting in a wine red-to-royal purple color shift (Figure 9C). The assay achieved a LOD of 0.38 $\mu\text{g/L}$ under optimal conditions (pH 10, 1-min incubation, 0.15 M NaCl) and demonstrated high selectivity with minimal interference from other compounds [93]. A simple and rapid colorimetric sensor has been developed for the detection of tetramethylthiuram disulfide (thiram) based on the anti-aggregation of AuNPs. The detection mechanism relies on 4-aminothiophenol-functionalized AuNPs, where the thiol group anchors to the AuNP surface, and the amine group coordinates with Ag^+ , inducing aggregation. However, in the presence of thiram, its strong binding affinity for Ag^+ captures the ions, preventing AuNP aggregation and restoring the original red color (Figure 9D). This system enables naked-eye detection within 15 min, with a detection limit of 0.04 μM . The sensor demonstrates high selectivity against other pesticides and metal ions and has been successfully applied to apple and soil samples [94].

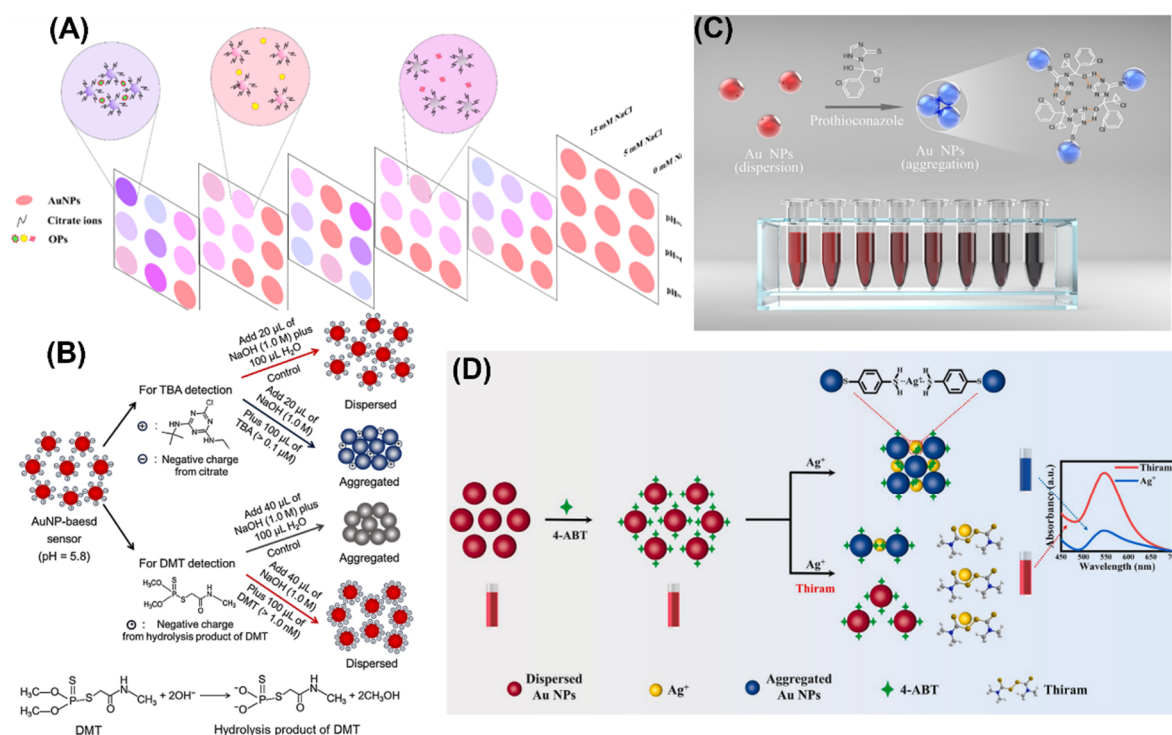


Figure 9. Colorimetric sensing strategies for pesticide and fungicide detection using AuNP-based probes. (A) Diagram of a colorimetric sensor array and detection principle for OPs based on citrate-stabilized AuNPs. Reproduced with permission [91]. Copyright 2016, American Chemical Society. (B) Schematic illustration of the detection mechanism for TBA and DMT, along with the reaction equation of DMT under alkaline conditions. Reproduced with permission [92]. Copyright 2018, Elsevier. (C) Prothioconazole-induced colorimetric response of AuNPs. Reproduced with permission [93]. Copyright 2020, American Chemical Society. (D) Schematic illustration of thiram detection using 4-aminothiophenol-functionalized AuNPs. Reproduced with permission [94]. Copyright 2022, Elsevier.

4.2. Detection of Veterinary Drug Residues

Clenbuterol, a strictly regulated growth promoter in livestock, can contaminate meat products and pose serious health risks to consumers, including cardiovascular complications, and metabolic disturbances [95,96].

A rapid and selective colorimetric sensor for CB detection has been developed using cysteamine-modified AuNPs. In this system, the thiol group of cysteamine binds to the AuNP surface, while the amine group remains exposed, enabling hydrogen bonding interactions with the hydroxyl, chloride, and amine groups of clenbuterol. These interactions induce AuNP aggregation, leading to a wine red-to-blue-gray color change, which is detectable by naked-eye observation or UV-vis spectroscopy. This sensor achieves a detection limit of 50 nM, demonstrating excellent selectivity against common food components [97]. Similarly, melamine-functionalized AuNPs have been employed for CB detection, where hydrogen bonding interactions between CB and melamine trigger AuNP aggregation, resulting in a wine red-to-blue color shift (Figure 10A). This method achieves an ultra-low detection limit of 2.8×10^{-11} M, offering a highly sensitive and cost-effective approach for clenbuterol analysis [39].

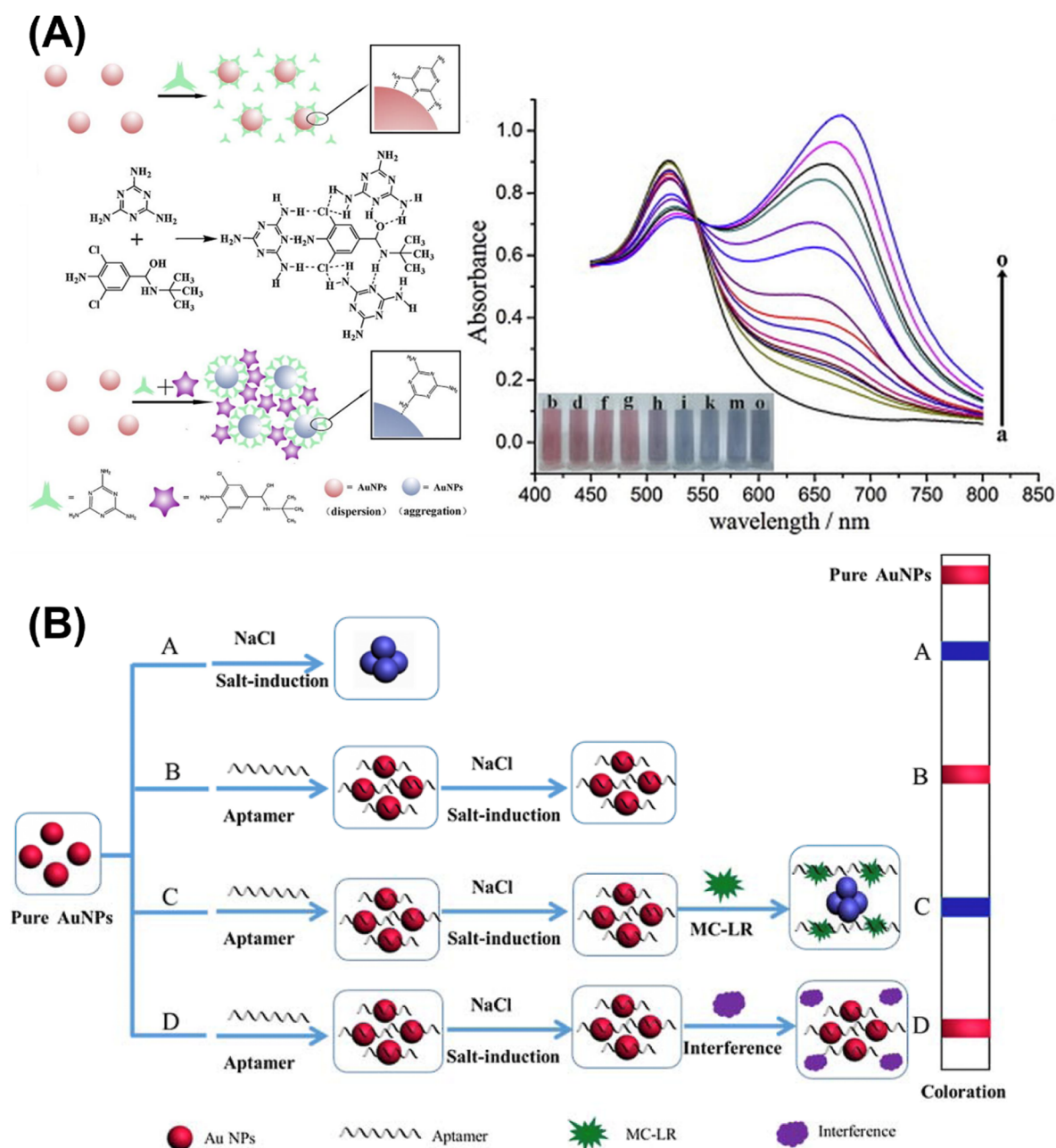


Figure 10. Colorimetric sensing strategies for CB and microcystin-LR using AuNP-based systems. (A) Left: Schematic illustration of the detection procedure for CB using melamine functionalized AuNPs. Right: UV-vis absorption spectra of AuNPs after the addition of CB of varying concentrations. Reproduced with permission [39]. Copyright 2012, Elsevier. (B) Schematic representation of the colorimetric sensing mechanism for the analytical determination of microcystin-LR. Reproduced with permission [106]. Copyright 2015, Elsevier.

4.3. Detection of Antibiotics

Antibiotics enter the environment through pharmaceutical waste, livestock runoff, and wastewater discharge, leading to contamination of soil and water systems [98,99]. Their persistent presence promotes the development of antibiotic-resistant bacteria, posing serious risks to ecosystems and public health by reducing the effectiveness of essential medical treatments [100].

Hydrogen bonding interactions are also utilized for antibiotic detection. Kanamycin, an aminoglycoside antibiotic, contains multiple amino and hydroxyl groups capable of forming hydrogen bonds. To exploit this property, AuNPs are functionalized with 4-amino-3-hydrazino-5-mercapto-1,2,4-triazole (AHMT), where the thiol group anchors onto the AuNP surface. Upon kanamycin addition, hydrogen bonding interactions between kanamycin and AHMT facilitate nanoparticle aggregation, leading to a visible red-to-deep purple color shift. This sensor achieves a detection limit of 0.004 μM , demonstrating high sensitivity and selectivity [101]. Another approach to detect antibiotics is using aptamers. The AuNPs are first stabilized with aptamers in high salt condition

while with the tetracycline (TET) and chloramphenicol (CAP), the antibiotics selectively bind to aptamers and this binding reduces the aptamer's ability to stabilize the AuNPs, leading to the detachment of the recognized fragment and subsequent AuNP aggregation causing aggregation in high-salt conditions. The sensor demonstrates high selectivity and sensitivity, achieving detection limits of 32.9 nM for TET and 7.0 nM for CAP [102].

4.4. Detection of Industrial and Natural Contaminants in Food and Water

Microcystin-LR is a potent hepatotoxin produced by cyanobacteria in contaminated water sources [103]. T-2 toxin is a mycotoxin from *Fusarium* fungi, contaminating food and feed, causing immunotoxic and cytotoxic effects [104]. Bisphenol A (BPA) is an industrial chemical used in plastics, acting as an endocrine disruptor with potential health risks [105].

Aptamers can also be utilized for both natural toxins and chemical contaminants detection. In this approach, aptamers first stabilize AuNPs in a high-salt environment, preventing aggregation. Upon introduction of target, the aptamers selectively bind to their targets, undergo conformational changes, and detach from the AuNP surface, triggering nanoparticle aggregation and a visible color shift (Figure 10B). This method enables the detection of microcystin-LR (LOD: 0.37 nM) [106], T-2 toxin (LOD: 57.8 pg/mL) [107], and bisphenol A (LOD: 0.004 nM) [108], demonstrating high sensitivity and specificity.

Azodicarbonamide (ADA), used as a food additive and dough conditioner, can contribute to environmental pollution through industrial emissions and wastewater discharge, potentially forming harmful byproducts that impact air and water quality [109]. ADA can be detected using an anti-aggregation mechanism. Unlike previously introduced methods, GSH is used to induce AuNP aggregation post-synthesis. GSH binds to AuNP surfaces via Au–S bonding, while its zwitterionic groups promote aggregation through electrostatic interactions. Upon introduction of ADA, GSH undergoes oxidation, leading to thiol dimerization and the formation of glutathione disulfide. This modification prevents GSH from cross-linking AuNPs, reducing aggregation and restoring the red color. The sensor achieves a visual detection limit of 0.33 μM (38.3 ppb) and a spectrophotometric detection limit of 0.23 μM (26.7 ppb) [110].

4.5. Detection of Formaldehyde

Formaldehyde (HCHO) is a toxic environmental pollutant commonly released from industrial emissions, building materials, and household products [111]. It poses serious health risks, including respiratory irritation, allergic asthma, and increased cancer risk with long-term exposure [112].

An ultra-sensitive colorimetric sensor for HCHO was developed based on its ability to reduce Ag^+ , forming Au@Ag core-shell nanorods. Ag^0 selectively deposits on the tips of AuNRs, where CTAB shields the sides, increasing the aspect ratio and inducing a redshift in the longitudinal plasmon band accompanied by a visible color change. The sensor achieves a detection limit as low as 6.3×10^{-11} g/mL, offering a rapid, label-free, and selective method suitable for on-site environmental monitoring [32].

5. Colorimetric Sensors Beyond AuNPs

Although AuNPs are the most used plasmonic materials in colorimetric sensors, other plasmonic nanoparticles, such as silver and copper nanoparticles (AgNPs and CuNPs), have also been explored. AgNPs exhibit a color change from yellow to red upon aggregation and, like AuNPs, citrate-capped AgNPs have been used to detect Ni^{2+} via crosslinking-induced aggregation [113]. Similarly, GSH-capped AgNPs show Ni^{2+} -induced aggregation behavior [114]. Green-synthesized AgNPs have also demonstrated detection capability for ions such as Hg^{2+} , Pb^{2+} , and Zn^{2+} [115]. In the case of Cu, L-cysteine [116] and citrate-capped nanoparticles [117] have been used for Hg^{2+} detection. Together, AgNPs and CuNPs expand the colorimetric sensing toolkit beyond AuNPs, enabling complementary detection strategies for environmental pollutants.

In addition to plasmonic nanosensors, other colorimetric sensing strategies have also been widely explored for environmental pollutant detection. Intramolecular charge transfer transitions enable highly selective sensing of Cu^{2+} , resulting in a visible color change from yellow to blue [118]. Fluorescence resonance energy transfer between donor and acceptor molecules allows for highly sensitive detection of Hg^{2+} , accompanied by a shift from greenish-yellow to orange [119]. Specific recognition between small-molecule ligands and various metal ions enables distinct color responses for multimetal ion identification [120]. Fluorescence quenching between Fe^{3+} and nitrogen-doped graphene quantum dots demonstrates excellent sensitivity and selectivity [121]. Metal-organic frameworks with nitro-functionalized linkers also show promise as dual-mode sensors, exhibiting luminescent turn-off or turn-on responses for MnO_4^- and Hg^{2+} , respectively [122]. The synthesis routes and detection mechanisms of these sensors vary significantly from system to system. In contrast, most AuNP-based

colorimetric sensors rely on aggregation-induced color change, with AuNPs serving as readily available and tunable templates. Notably, many non-plasmonic colorimetric sensors incorporate fluorescence-based detection, often requiring UV illumination for visual readout. In these systems, the design and synthesis of the sensing molecule play a central role in performance. Additionally, non-plasmonic systems often produce a wider range of color transitions, whereas AuNP-based sensors typically shift from red to purple (or vice versa). While differing in mechanism and design, these sensor types offer complementary strengths, and integrating plasmonic platforms with other colorimetric approaches may further enhance the performance and adaptability of future sensing systems.

6. Summary and Outlook

AuNP-based colorimetric sensing has emerged as a powerful platform for the rapid, sensitive, and visual detection of a wide range of analytes. This review highlights the diverse mechanisms underlying AuNP-based colorimetric sensing, including aggregation-based strategies such as classical aggregation, anti-aggregation, and ligand exchange, along with non-aggregation mechanisms like growth and etching, which alter the optical properties of AuNPs through changes in size, shape, or surface composition. These approaches enable the detection of various inorganic species, such as metal ions and anions, as well as organic targets, including pesticides, antibiotics, industrial additives, and toxins. Table 1 summarizes the key sensing attributes of representative colorimetric nanosensors, including analyte type, LOD, dynamic range, selectivity, response time, and notable sensor characteristics. The strength of AuNP-based sensors lies in their simplicity, low cost, and ease of interpretation via visible color changes without the need for sophisticated instrumentation. Furthermore, the surface chemistry of AuNPs is highly adaptable, allowing selective recognition through various chemistries and providing a flexible foundation for designing highly tailored sensing systems.

Despite significant advances, several practical challenges remain. While many sensing systems claim selectivity, most studies still rely on simplified interference tests with metal ion mixtures, and only a few have demonstrated reliable performance in complex sample matrices such as milk, urine, or paint extracts. Additionally, although the visual nature of colorimetric sensing is appealing, quantifying subtle color variations remains difficult without external instrumentation. Some approaches address this by incorporating smartphone-based RGB analysis, UV-vis spectrometry, or even fluorescence and DLS—but these additions often compromise the simplicity that makes colorimetric methods attractive in the first place. Lowering the detection limit has been a major focus, with aptamer-based sensors showing impressive sensitivity. However, the high cost and structural complexity of DNA-based components limit their widespread application.

Looking ahead, more efforts should focus on bridging the gap between laboratory demonstrations and real-world usability. Many studies still lack rigorous validation in real sample matrices, and reproducibility is often underreported or unsupported by statistical analysis. While colorimetric methods are valued for their simplicity, consistently and quantitatively interpreting color changes remains challenging. Current strategies using RGB values or UV-vis absorbance ratios can be inconsistent or dependent on lighting and instrumentation. To address this, incorporating hue-based color models could provide a more standardized approach to quantifying visual responses [24]. Future work should emphasize developing robust, low-cost, and user-friendly analysis tools—such as smartphone apps with hue extraction—and validating sensor performance under practical conditions.

Overall, AuNP-based colorimetric sensing remains a dynamic and evolving field with broad potential across environmental monitoring, food safety, and beyond. Realizing its full potential will depend on continued innovation in surface chemistry, signal quantification, and device integration—ultimately paving the way for practical, on-site, and user-friendly sensing solutions.

Table 1. Key sensing attributes of representative sensors.

Refs.	Analytes	LOD	Dynamic Range	Selectivity Over	Response Time	Features/Limitations
[41]	Pb ²⁺	0.1 μM	100 nM–4 μM	Mg ²⁺ , Ca ²⁺ , Mn ²⁺ , Co ²⁺ , Ni ²⁺ , Cu ²⁺ , Zn ²⁺ , Cd ²⁺	2 h	Long incubation time
[42]	Pb ²⁺	0.4 μM	0.4–2 μM	Co ²⁺ , Zn ²⁺ , Cd ²⁺ , Mn ²⁺ , Ni ²⁺ , Ca ²⁺ , Mg ²⁺	10 min	High sensitivity; fast detection
[30]	Pb ²⁺	pH 7.2: 3 nM pH 5.5: 120 nM	pH 7.2: 3 nM–12 μM pH 5.5: 120 nM–20 μM	Zn ²⁺ , Mn ²⁺ , Co ²⁺ , Ni ²⁺ , Cd ²⁺ , Ca ²⁺ , Mg ²⁺ , Hg ²⁺	6 min	High sensitivity; label-free Au NPs
[25]	Pb ²⁺	18 μM	18–100 μM	Zn ²⁺ , Ni ²⁺ , Cu ²⁺ , Mg ²⁺ , Se ⁴⁺ , Cr ⁶⁺ , As ⁵⁺ , Hg ²⁺ , Fe ³⁺ , Al ³⁺ , Ca ²⁺ , Li ⁺ , Sn ²⁺ , Cd ²⁺	0 min	Low sensitivity; fast response
[35]	Pb ²⁺	100 nM	0.1–50 μM	Hg ²⁺ , Mg ²⁺ , Zn ²⁺ , Ni ²⁺ , Cu ²⁺ , Co ²⁺ , Ca ²⁺ , Mn ²⁺ , Fe ²⁺ , Cd ²⁺ , Ba ²⁺ , Cr ³⁺	0 min	Fast response
[36]	Pb ²⁺	100 ppt	100–25,000 ppt	Mg ²⁺ , Ca ²⁺ , Hg ²⁺ , Mn ²⁺ , Fe ²⁺ , Cu ²⁺ , Ni ²⁺ , Co ²⁺ , Zn ²⁺ , Cd ²⁺	20 min	High sensitivity (DLS-enabled)
[54]	Pb ²⁺	10 nM	10–1000 nM	Li ⁺ , Na ⁺ , K ⁺ , Mg ²⁺ , Ca ²⁺ , Sr ²⁺ , Ba ²⁺ , Mn ²⁺ , Fe ²⁺ , Fe ³⁺ , Co ²⁺ , Ni ²⁺ , Au ³⁺ , Cu ²⁺ , Zn ²⁺ , Cd ²⁺ , Hg ²⁺ , Pb ²⁺	20 min	High sensitivity; broad selectivity testing
[45]	Pb ²⁺	0.29 μM	80 ng/mL–25 μg/ml	Ni ²⁺ , Co ²⁺ , Mg ²⁺ , Ca ²⁺ , Zn ²⁺ , Fe ³⁺	5 min	Low sensitivity and selectivity
[55]	Pb ²⁺	16.7 nM	0.5–8 μM	Ag ⁺ , Al ³⁺ , Ca ²⁺ , Cd ²⁺ , Co ²⁺ , Cr ³⁺ , Cr ⁶⁺ , Cu ²⁺ , Fe ²⁺ , Fe ³⁺ , Hg ²⁺ , Mg ²⁺ , Mn ²⁺ , Ni ²⁺ , Pb ²⁺ , Zn ²⁺	10 min	High sensitivity
[58]	As ³⁺	1.8 ppb	4–100 ppb	K ⁺ , Cu ²⁺ , Mn ²⁺ , Zn ²⁺ , Mg ²⁺ , Na ⁺ , Hg ²⁺ , Fe ²⁺ , Fe ³⁺ , Ca ²⁺ , Ni ²⁺ , Pb ²⁺ , Cd ²⁺ , Cr ³⁺ , Al ³⁺ , As ⁵⁺ , CH ₄ AsNaO ₃ , (CH ₃) ₂ AsO ₂ H	6 min	High sensitivity via dialyzed citrate-Au NPs
[59]	As ³⁺	0.53 ppb	1–114 ppb	As ³⁺ , Pb ²⁺ , Co ²⁺ , Hg ²⁺ , Cd ²⁺ , Ni ²⁺ , Cu ²⁺	5 min	Green synthesis with glucose
[37]	As ³⁺	0.12 ppb	0.12–1 ppb	Fe ³⁺ , Co ²⁺ , Ni ²⁺ , K ⁺ , Na ⁺ , Mg ²⁺ , Ca ²⁺ , Cu ²⁺ , Hg ²⁺ , Pb ²⁺	1 h	RGB quantification; narrow range
[38]	As ⁵⁺ , As ³⁺	2.5 μg/L	0.25–20 μg/L	Cu ²⁺ , Ni ²⁺ , Co ²⁺ , Ca ²⁺ , Mg ²⁺ , Na ⁺	N/A	As ⁵⁺ detection
[27]	As ³⁺	Mode D: 0.57 ppb Mode A: 0.41 ppb	Mode D: 2–240 ppb Mode A: 2–40 ppb	Pb ²⁺ , Ag ⁺ , Fe ³⁺ , Zn ²⁺ , Cd ²⁺ , Cu ²⁺ , Ni ²⁺ , Cr ³⁺ , Bi ³⁺ , K ⁺ , Na ⁺ , Mg ²⁺ , Al ³⁺ , Ba ²⁺ , Sn ²⁺ , Ca ²⁺ , As ⁵⁺ , CH ₄ AsNaO ₃ , (CH ₃) ₂ AsO ₂ H	35 min	High sensitivity
[26]	Hg ²⁺	2.8 nM	5 nM–1000 nM	Cd ²⁺ , Mg ²⁺ , Co ²⁺ , Zn ²⁺ , Pb ²⁺ , Mn ²⁺ , Ni ²⁺ , Cr ³⁺ , Cu ²⁺ , Fe ²⁺ , Fe ³⁺ , Na ⁺	5 min	Broad dynamic range
[28]	Hg ²⁺	50 nM	25–750 nM	Co ²⁺ , Mn ²⁺ , Pb ²⁺ , Ca ²⁺ , Cd ²⁺ , Cr ³⁺ , Zn ²⁺ , Cu ²⁺ , Ni ²⁺	40 min	Long incubation time
[62]	Hg ²⁺	0.15 nM	0.25–500 nM	Zn ²⁺ , Mg ²⁺ , Cu ²⁺ , Mn ²⁺ , Cd ²⁺ , Ni ²⁺ , Pb ²⁺	3 min	High sensitivity
[63]	Hg ²⁺ , CH ₃ Hg ⁺	Hg ²⁺ : 10 nM CH ₃ Hg ⁺ : 15 nM	Hg ²⁺ : 10 nM–1.5 μM CH ₃ Hg ⁺ : 15 nM–0.8 μM	Cd ²⁺ , Pb ²⁺ , Mg ²⁺ , Mn ²⁺ , Co ²⁺ , Ba ²⁺ , Zn ²⁺ , Ag ⁺	2 min	CH ₃ Hg ⁺ detection
[64]	Hg ²⁺	5 μM	N/A	Cu ²⁺ , Zn ²⁺ , Co ²⁺ , Mg ²⁺ , Ni ²⁺ , Ba ²⁺	20 min	Low sensitivity
[34]	Al ³⁺	1 μM	N/A	Hg ²⁺ , Fe ³⁺ , Cd ²⁺ , Ag ⁺ , Cu ²⁺ , Ni ²⁺ , Zn ²⁺ , Mn ²⁺ , Co ²⁺ , Pb ²⁺ , Al ³⁺	0 min	Low sensitivity; fast response; Sb ³⁺ /Cr ³⁺ interference
[67]	Al ³⁺	0.81 μM	1–3.5 μM	Ag ⁺ , Mg ²⁺ , Ca ²⁺ , Mn ²⁺ , Co ²⁺ , Ni ²⁺ , Cu ²⁺ , Zn ²⁺ , Cd ²⁺ , Hg ²⁺ , Pb ²⁺ , Fe ²⁺ , Fe ³⁺ , Cr ³⁺	1 min	Narrow dynamic range
[68]	Al ³⁺	1.15 μM	1.15–12 μM	K ⁺ , Ag ⁺ , Na ⁺ , Ba ²⁺ , Cd ²⁺ , Ca ²⁺ , Cu ²⁺ , Pb ²⁺ , Mn ²⁺ , Mg ²⁺ , Hg ²⁺ , Ni ²⁺ , Pt ²⁺ , Sn ²⁺ , Zn ²⁺ , Al ³⁺ , Co ³⁺ , Cr ³⁺ , Au ³⁺ , Fe ³⁺	1 min	Low sensitivity
[69]	Al ³⁺	0.29 μM	9–23 μM	Ag ⁺ , Cd ²⁺ , Co ²⁺ , Al ³⁺ , Cr ³⁺ , Cu ²⁺ , Fe ³⁺ , Hg ²⁺ , Mg ²⁺ , Mn ²⁺ , Ni ²⁺ , Pb ²⁺ , Ba ²⁺ , Zn ²⁺	10 s	Relatively high sensitivity
[71]	Cs ⁺	19 μM	19–70 μM	Li ⁺ , Na ⁺ , K ⁺ , Ca ²⁺ , Al ³⁺ , Mn ²⁺ , Fe ²⁺ , Mg ²⁺ , NH ₄ ⁺ , PO ₄ ³⁻ , Cl ⁻	23 min	Low sensitivity
[73]	Ag ⁺	50 nM	100–4000 nM	Cd ²⁺ , Fe ³⁺ , Ca ²⁺ , Mn ²⁺ , Cu ²⁺ , Co ²⁺ , Ni ²⁺ , Al ³⁺ , Zn ²⁺ , Pb ²⁺	10 min	High sensitivity
[75]	Tl ⁺	3.2 nM	0.01–0.6 μM	K ⁺ , Na ⁺ , Mg ²⁺ , Ca ²⁺ , Al ³⁺ , Co ²⁺ , Ni ²⁺ , Mn ²⁺ , Cu ²⁺ , Zn ²⁺ , Fe ³⁺ , Cr ³⁺ , Cd ²⁺ , Ag ⁺ , Pb ²⁺ , Hg ²⁺	10 min	High sensitivity
[78]	Sc ³⁺	0.02 μM	0.1–3 μM	Ce ³⁺ , Pr ³⁺ , Nd ³⁺ , Sm ³⁺ , Eu ³⁺ , Gd ³⁺ , Tb ³⁺ , Dy ³⁺ , Ho ³⁺ , Er ³⁺ , Tm ³⁺ , Yb ³⁺ , Lu ³⁺ , Y ³⁺ , La ³⁺	1 min	Narrow dynamic range
[81]	CN ⁻	0.1 μM	0.1–50 μM	Cl ⁻ , Br ⁻ , BrO ₃ ³⁻ , C ₆ H ₅ O ₇ ⁻ , NO ₃ ⁻ , CO ₃ ²⁻ , PO ₄ ³⁻ , F ⁻ , SO ₃ ²⁻ , S ₂ O ₈ ²⁻ , SO ₄ ²⁻ , ClO ₄ ⁻ , CH ₃ COO ⁻ , Li ⁺ , Mg ²⁺ , K ⁺ , Ca ²⁺ , Cr ³⁺ , Mn ²⁺ , Fe ²⁺ , Co ²⁺ , Ni ²⁺ , Cu ²⁺ , Cd ²⁺ , Zn ²⁺ , Hg ²⁺ , Pb ²⁺	30 min	High selectivity
[31]	NO ₂ ⁻	4 μM	1.0–15.0 μM	NO ₃ ⁻ , SO ₄ ²⁻ , PO ₄ ³⁻ , Ac ⁻ , Br ⁻ , SCN ⁻ , ClO ₄ ⁻ , S ²⁻ , Cu ²⁺ , Pb ²⁺ , Mg ²⁺ , Hg ²⁺ , Cd ²⁺ , Zn ²⁺ , Al ³⁺ , Mn ²⁺ , Ag ⁺ , Cr ³⁺	10 min	Narrow dynamic range
[84]	Hg ²⁺ , Cd ²⁺ , Fe ³⁺ , Pb ²⁺ , Al ³⁺ , Cu ²⁺ , Cr ³⁺	Pb ²⁺ , Hg ²⁺ : 2 μM Fe ³⁺ : 10 μM	2–50 μM	Ag ⁺ , Ca ²⁺ , Zn ²⁺ , Co ²⁺ , Ni ²⁺ , Sr ²⁺ , K ⁺ , Na ⁺ , Fe ²⁺	15 min	Multi-metal-ion discrimination; Low sensitivity

Table 1. Cont.

Refs.	Analytes	LOD	Dynamic Range	Selectivity Over	Response Time	Features/Limitations
[85]	Ti ⁴⁺ , Cr ³⁺ , Mn ²⁺ , Pb ²⁺ , Sn ⁴⁺ , Fe ³⁺	100 nM for all	Ti ⁴⁺ , Cr ³⁺ , Mn ²⁺ , Pb ²⁺ : 100–900 nM Sn ⁴⁺ : 100–1000 nM Fe ³⁺ : 100–800 nM	N/A	20 min	No selectivity testing
[86]	Ba ²⁺ , Cd ²⁺ , Pb ²⁺	Ba ²⁺ : 20 nM Cd ²⁺ : 20 nM Pb ²⁺ : 50 nM	Ba ²⁺ : 0.02–22 μM Cd ²⁺ : 0.02–10 μM Pb ²⁺ : 0.05–10 μM	NH ₄ ⁺ , SO ₄ ²⁻ , CO ₃ ²⁻ , PO ₄ ³⁻ , Al ³⁺ , Zn ²⁺ , Cs ⁺ , Rb ⁺ , K ⁺ , Li ⁺ , Fe ³⁺ , Fe ²⁺ , Na ⁺ , Mg ²⁺ , Cu ²⁺ , Ni ²⁺ , Ca ²⁺ , Mn ²⁺ , Co ²⁺ , Cr ³⁺	20 min	Cannot differentiate individual cation; high sensitivity
[40]	Pb ²⁺ , Cu ²⁺	0.65 ppm Cu ²⁺ 10.0 ppm Pb ²⁺	N/A	Li ⁺ , Na ⁺ , K ⁺ , Ba ²⁺ , Mg ²⁺ , Fe ³⁺ , Cs ⁺ , Hg ²⁺ , Ca ²⁺ , Zn ²⁺ , Cd ²⁺ , Ni ²⁺ , Sr ²⁺ , Cu ²⁺ , Pb ²⁺	N/A	Pb ²⁺ vs Cu ²⁺ color different; range not reported
[87]	Hg ²⁺ , Pb ²⁺ , Cu ²⁺	200 nM for all	0.2–1 μM	Ba ²⁺ , Ca ²⁺ , Cd ²⁺ , Co ²⁺ , Fe ³⁺ , Mg ²⁺ , Mn ²⁺ , Ni ²⁺ , Zn ²⁺	N/A	Cannot differentiate individual ions
[91]	Azinphosmethyl (AM) Chlorpyrifos (CP) Fenamiphos (FP) Pirimiphosmethyl (PM) Phosalone (PS)	AM: 7 ng/mL CP: 118 ng/mL FP: 7 ng/mL PM: 30 ng/mL PS: 37 ng/mL	AM: 80–400 ng/mL CP: 12–800 ng/mL FP: 80–400 ng/mL PM: 40–800 ng/mL PS: 40–320 ng/mL	carbaryl, carbofuran, methiocarb, pirimicarb, imidacloprid, thiamethoxam, tebuconazole, propiconazole	10 min	Simultaneous detection and discrimination
[29]	Acephate (AC) Phenthoate (PT) Profenofos (PF) Acetamiprid (AP) Chlorothalonil (CT) Cartap	AC: 3.46 × 10 ⁻⁷ M PT: 3.0 × 10 ⁻⁹ M PF: 6.0 × 10 ⁻⁷ M AP: 6.24 × 10 ⁻¹⁰ M CT: 3.75 × 10 ⁻⁷ M Cartap: 1.7 × 10 ⁻⁸ M	AC: 10–900 μM PT: 0.01–1.50 μM PF: 1.0–200 μM AP: 0.001–0.15 μM CT: 1.0–1000 μM Cartap: 0.05–1.50 μM	Na ⁺ , K ⁺ , Cu ²⁺ , Zn ²⁺ , Cd ²⁺ , Fe ²⁺ , Mn ²⁺ , Mg ²⁺ , Ba ²⁺ , Cr ³⁺ , Fe ³⁺ , Al ³⁺ , Cl ⁻ , I ⁻ , Br ⁻ , NO ₃ ⁻ , SO ₄ ²⁻ , Cr ₂ O ₇ ²⁻	5 min	High selectivity
[92]	TBA, DMT	TBA: 0.02 μM DMT: 6.2 nM	TBA: 0.1–0.9 μM DMT: 1–40 nM	30 kinds of environmental pollutants	5 min	Broad selectivity testing
[93]	Prothioconazole	0.38 μg/L	1.33–19.99 μg/L	prothioconazole-desthio, fluxapyroxad, fluazinam, azoxystrobin, metconazole, pyraclostrobin, methoxone, diflubenzuron and cyazofamid, thiodicarb	1 min	High sensitivity; fast response
[94]	Thiram	0.04 μM	0.05–2.0 μM	ethametsulfuron, diniconazole, thiophanate, gibberellins, dinotefuran, 2mercaptobenzothiazole, nereistoxin oxalate.	12 min	Low sensitivity, narrow range
[97]	CB	0.05 μM	0.05–1 μM	alamime, phenylalanine, glycerol, vitamin, threonine, urea, cysteamine, glucose, glycine, NaCl, CaCl ₂	15 min	Low sensitivity, narrow range
[39]	CB	2.8 × 10 ⁻¹¹ M	2.8 × 10 ⁻¹⁰ –1.4 × 10 ⁻⁶ M	DL-epinephrine, phenylalanine, tryptohan, alamine, uric acid, glycine, glycerol, glucose, MgCl ₂ , CaCl ₂ , NaCl	2 min	Broad range, fast response
[106]	Microcystin-LR	0.37 nM	0.5 nM–7.5 μM	acetaminprid, glyphosate, dylox, atrazine, clofentezine	15 min	Broad dynamic range, high sensitivity
[107]	T-2 toxin	57.8 pg/mL	0.1 ng/mL–5000 ng/mL	aflatoxins B1, ochratoxin A, zearalenone, fumonisin B	40 min	Broad dynamic range, high sensitivity, long incubation time
[108]	Bisphenol A	1 pg/mL	0.001–1000 ng/mL	bisphenol B, bisphenol C, diphenolic acid, bisphenol AF	40 min	Broad dynamic range, high sensitivity, long incubation time
[110]	Azodicarbonamide	0.23 μM	0.12 μM–1.00 μM	dibenzoyl peroxide, potassium bromate, cysteine	2 h	Short dynamic range, low selectivity, long incubation time

Author Contributions: X.Z.: Conceptualization, Writing—original draft, Writing—review & editing. A.G.K.: Writing—review & editing. Y.Y.: Conceptualization, Writing—review & editing. All authors have read and agreed to the published version of the manuscript

Funding: This research was funded by the Office of Research and Economic Development (RED) at the University of California, Riverside, through the SoCal OASIS Internal Funding Award.

Data Availability Statement: Not applicable.

Acknowledgments: We thank the Office of Research and Economic Development (RED) at the University of California, Riverside, for the SoCal OASIS Internal Funding Award.

Declaration of Generative AI and AI-assisted Technologies in the Writing Process: During the preparation of this work, the authors used ChatGPT 4o to improve the clarity and readability of the manuscript. After using this tool, the authors reviewed and edited the content as needed and take full responsibility for the content of the publication.

Conflicts of Interest: The authors declare no conflict of interest.

References

1. Sumaira; Siddique, H.M.A. Industrialization, energy consumption, and environmental pollution: Evidence from South Asia. *Environ. Sci. Pollut. Res.* **2023**, *30*, 4094–4102. <https://doi.org/10.1007/s11356-022-22317-0>.
2. Lin, L.; Yang, H.; Xu, X. Effects of Water Pollution on Human Health and Disease Heterogeneity: A Review. *Front. Environ. Sci.* **2022**, *10*, 880246. <https://doi.org/10.3389/fenvs.2022.880246>.
3. Wen, Y.; Schoups, G.; van de Giesen, N. Organic pollution of rivers: Combined threats of urbanization, livestock farming and global climate change. *Sci. Rep.* **2017**, *7*, 43289. <https://doi.org/10.1038/srep43289>.
4. Boyd, R.S. Heavy metal pollutants and chemical ecology: Exploring new frontiers. *J. Chem. Ecol.* **2010**, *36*, 46–58. <https://doi.org/10.1007/s10886-009-9730-5>.
5. Lipczynska-Kochany, E. Humic substances, their microbial interactions and effects on biological transformations of organic pollutants in water and soil: A review. *Chemosphere* **2018**, *202*, 420–437. <https://doi.org/10.1016/j.chemosphere.2018.03.104>.
6. Zhu, Z.-Y.; Zhang, J.; Wu, Y.; Zhang, Y.-Y.; Lin, J.; Liu, S.-M. Hypoxia off the Changjiang (Yangtze River) Estuary: Oxygen depletion and organic matter decomposition. *Mar. Chem.* **2011**, *125*, 108–116. <https://doi.org/10.1016/j.marchem.2011.03.005>.
7. Santos, F.J.; Galceran, M.T. The application of gas chromatography to environmental analysis. *Trends Anal. Chem.* **2002**, *21*, 672–685.
8. Richardson, S.D. Environmental Mass Spectrometry: Emerging Contaminants and Current Issues. *Anal. Chem.* **2008**, *80*, 4373–4402.
9. Pohl, P. Determination of metal content in honey by atomic absorption and emission spectrometries. *Trends Anal. Chem.* **2009**, *28*, 117–128. <https://doi.org/10.1016/j.trac.2008.09.015>.
10. Rekhi, H.; Rani, S.; Sharma, N.; Malik, A.K. A Review on Recent Applications of High-Performance Liquid Chromatography in Metal Determination and Speciation Analysis. *Crit. Rev. Anal. Chem.* **2017**, *47*, 524–537. <https://doi.org/10.1080/10408347.2017.1343659>.
11. Liu, B.; Zhuang, J.; Wei, G. Recent advances in the design of colorimetric sensors for environmental monitoring. *Environ. Sci. Nano* **2020**, *7*, 2195–2213. <https://doi.org/10.1039/d0en00449a>.
12. Wei, H.; Hossein Abtahi, S.M.; Vikesland, P.J. Plasmonic colorimetric and SERS sensors for environmental analysis. *Environ. Sci. Nano* **2015**, *2*, 120–135. <https://doi.org/10.1039/c4en00211c>.
13. Tang, L.; Li, J. Plasmon-Based Colorimetric Nanosensors for Ultrasensitive Molecular Diagnostics. *ACS Sens.* **2017**, *2*, 857–875. <https://doi.org/10.1021/acssensors.7b00282>.
14. Balasubramanian, S.K.; Yang, L.; Yung, L.Y.; Ong, C.N.; Ong, W.Y.; Yu, L.E. Characterization, purification, and stability of gold nanoparticles. *Biomaterials* **2010**, *31*, 9023–9030. <https://doi.org/10.1016/j.biomaterials.2010.08.012>.
15. Willets, K.A.; Van Duyne, R.P. Localized surface plasmon resonance spectroscopy and sensing. *Annu. Rev. Phys. Chem.* **2007**, *58*, 267–297. <https://doi.org/10.1146/annurev.physchem.58.032806.104607>.
16. Link, S.; El-Sayed, M.A. Spectral Properties and Relaxation Dynamics of Surface Plasmon Electronic Oscillations in Gold and Silver Nanodots and Nanorods. *J. Phys. Chem. B* **1999**, *103*, 8410–8426.
17. Kelly, K.L.; Coronado, E.; Zhao, L.L.; Schatz, G.C. The Optical Properties of Metal Nanoparticles: The Influence of Size, Shape, and Dielectric Environment. *J. Phys. Chem. B* **2003**, *107*, 668–677.
18. Gao, C.; Vuong, J.; Zhang, Q.; Liu, Y.; Yin, Y. One-step seeded growth of Au nanoparticles with widely tunable sizes. *Nanoscale* **2012**, *4*, 2875–2878. <https://doi.org/10.1039/c2nr30300k>.
19. Huang, X.; El-Sayed, M.A. Gold nanoparticles: Optical properties and implementations in cancer diagnosis and photothermal therapy. *J. Adv. Res.* **2010**, *1*, 13–28. <https://doi.org/10.1016/j.jare.2010.02.002>.
20. Zeng, J.; Zhang, Y.; Zeng, T.; Aleisa, R.; Qiu, Z.; Chen, Y.; Huang, J.; Wang, D.; Yan, Z.; Yin, Y. Anisotropic plasmonic nanostructures for colorimetric sensing. *Nano Today* **2020**, *32*, 100855. <https://doi.org/10.1016/j.nantod.2020.100855>.
21. Murphy, C.J.; Sau, T.K.; Gole, A.M.; Orendorff, C.J.; Gao, J.; Gou, L.; Hunyadi, S.E.; Li, T. Anisotropic Metal Nanoparticles: Synthesis, Assembly, and Optical Applications. *J. Phys. Chem. B* **2005**, *109*, 13857–13870.
22. Zhong, Z.; Patskovskyy, S.; Bouvrette, P.; Luong, J.H.T.; Gedanken, A. The Surface Chemistry of Au Colloids and Their Interactions with Functional Amino Acids. *J. Phys. Chem. B* **2004**, *108*, 4046–4052.
23. Jain, P.K.; Huang, W.; El-Sayed, M.A. On the Universal Scaling Behavior of the Distance Decay of Plasmon Coupling in Metal Nanoparticle Pairs: A Plasmon Ruler Equation. *Nano Lett.* **2007**, *7*, 2080–2088.

24. Montano-Priede, J.L.; Sanroman-Iglesias, M.; Zabala, N.; Grzelczak, M.; Aizpurua, J. Robust Rules for Optimal Colorimetric Sensing Based on Gold Nanoparticle Aggregation. *ACS Sens.* **2023**, *8*, 1827–1834. <https://doi.org/10.1021/acssensors.3c00287>.
25. Tripathi, R.M.; Park, S.H.; Kim, G.; Kim, D.-H.; Ahn, D.; Kim, Y.M.; Kwon, S.J.; Yoon, S.-Y.; Kang, H.J.; Chung, S.J. Metal-induced redshift of optical spectra of gold nanoparticles: An instant, sensitive, and selective visual detection of lead ions. *Int. Biodeter. Biodegr.* **2019**, *144*, 104740. <https://doi.org/10.1016/j.ibiod.2019.104740>.
26. Chen, L.; Lou, T.; Yu, C.; Kang, Q.; Chen, L. N-1-(2-mercaptoethyl)thymine modification of gold nanoparticles: A highly selective and sensitive colorimetric chemosensor for Hg²⁺. *Analyst* **2011**, *136*, 4770–4773. <https://doi.org/10.1039/c1an15585g>.
27. Zhang, D.; Chu, S.; Wang, L.; Zhan, X.; Zhou, P.; Zhang, D. Dual-mode colorimetric determination of As(III) based on negatively-charged aptamer-mediated aggregation of positively-charged AuNPs. *Anal. Chim. Acta* **2022**, *1221*, 340111. <https://doi.org/10.1016/j.aca.2022.340111>.
28. Chen, G.H.; Chen, W.Y.; Yen, Y.C.; Wang, C.W.; Chang, H.T.; Chen, C.F. Detection of mercury(II) ions using colorimetric gold nanoparticles on paper-based analytical devices. *Anal. Chem.* **2014**, *86*, 6843–6849. <https://doi.org/10.1021/ac5008688>.
29. Rana, K.; Bhamore, J.R.; Rohit, J.V.; Park, T.-J.; Kailasa, S.K. Ligand exchange reactions on citrate-gold nanoparticles for a parallel colorimetric assay of six pesticides. *New J. Chem.* **2018**, *42*, 9080–9090. <https://doi.org/10.1039/c8nj01294f>.
30. Wang, Z.; Lee, J.H.; Lu, Y. Label-Free Colorimetric Detection of Lead Ions with a Nanomolar Detection Limit and Tunable Dynamic Range by using Gold Nanoparticles and DNAzyme. *Adv. Mater.* **2008**, *20*, 3263–3267. <https://doi.org/10.1002/adma.200703181>.
31. Chen, Z.; Zhang, Z.; Qu, C.; Pan, D.; Chen, L. Highly sensitive label-free colorimetric sensing of nitrite based on etching of gold nanorods. *Analyst* **2012**, *137*, 5197–5200. <https://doi.org/10.1039/c2an35787a>.
32. Lin, J.-M.; Huang, Y.-Q.; Liu, Z.-b.; Lin, C.-Q.; Ma, X.; Liu, J.-M. Design of an ultra-sensitive gold nanorod colorimetric sensor and its application based on formaldehyde reducing Ag⁺. *RSC Adv.* **2015**, *5*, 99944–99950. <https://doi.org/10.1039/c5ra16266a>.
33. Park, J.W.; Shumaker-Parry, J.S. Structural study of citrate layers on gold nanoparticles: Role of intermolecular interactions in stabilizing nanoparticles. *J Am Chem Soc* **2014**, *136*, 1907–1921. <https://doi.org/10.1021/ja4097384>.
34. Chen, S.; Fang, Y.M.; Xiao, Q.; Li, J.; Li, S.B.; Chen, H.J.; Sun, J.J.; Yang, H.H. Rapid visual detection of aluminium ion using citrate capped gold nanoparticles. *Analyst* **2012**, *137*, 2021–2023. <https://doi.org/10.1039/c2an35129c>.
35. Chai, F.; Wang, C.; Wang, T.; Li, L.; Su, Z. Colorimetric detection of Pb²⁺ using glutathione functionalized gold nanoparticles. *ACS Appl. Mater. Interfaces* **2010**, *2*, 1466–1470. <https://doi.org/10.1021/am100107k>.
36. Beqa, L.; Singh, A.K.; Khan, S.A.; Senapati, D.; Arumugam, S.R.; Ray, P.C. Gold nanoparticle-based simple colorimetric and ultrasensitive dynamic light scattering assay for the selective detection of Pb(II) from paints, plastics, and water samples. *ACS Appl. Mater. Interfaces* **2011**, *3*, 668–673. <https://doi.org/10.1021/am101118h>.
37. Zheng, B.; Li, J.; Zheng, Z.; Zhang, C.; Huang, C.; Hong, J.; Li, Y.; Wang, J. Rapid colorimetric detection of arsenic (III) by glutathione functionalized gold nanoparticles based on RGB extracting system. *Opt. Laser Technol.* **2021**, *133*, 106522. <https://doi.org/10.1016/j.optlastec.2020.106522>.
38. Dominguez-Gonzalez, R.; Gonzalez Varela, L.; Bermejo-Barrera, P. Functionalized gold nanoparticles for the detection of arsenic in water. *Talanta* **2014**, *118*, 262–269. <https://doi.org/10.1016/j.talanta.2013.10.029>.
39. Zhang, X.; Zhao, H.; Xue, Y.; Wu, Z.; Zhang, Y.; He, Y.; Li, X.; Yuan, Z. Colorimetric sensing of clenbuterol using gold nanoparticles in the presence of melamine. *Biosens. Bioelectron.* **2012**, *34*, 112–117. <https://doi.org/10.1016/j.bios.2012.01.026>.
40. Ravi Gunupuru; Debdeep Maity; Gopala R Bhadu; Ashish Chakraborty; Srivastava, D.N.; Paul, P. Colorimetric detection of Cu²⁺ and Pb²⁺ ions using calix[4]arene functionalized gold nanoparticles. *J. Chem. Sci.* **2014**, *126*, 627–635.
41. Liu, J.; Lu, Y. A Colorimetric Lead Biosensor Using DNAzyme-Directed Assembly of Gold Nanoparticles. *J. Am. Chem. Soc.* **2003**, *125*, 6642–6643.
42. Liu, J.; Lu, Y. Accelerated Color Change of Gold Nanoparticles Assembled by DNAzymes for Simple and Fast Colorimetric Pb²⁺ Detection. *J. Am. Chem. Soc.* **2004**, *126*, 12298–12305.
43. Turkevich, J.; Stevenson, P.C.; Hillier, J. A study of the nucleation and growth processes in the synthesis of colloidal gold. *Discuss. Faraday Soc.* **1951**, *11*, 55–75.
44. Liu, D.; Wang, Z.; Jiang, X. Gold nanoparticles for the colorimetric and fluorescent detection of ions and small organic molecules. *Nanoscale* **2011**, *3*, 1421–1433. <https://doi.org/10.1039/c0nr00887g>.
45. Berlina, A.N.; Sharma, A.K.; Zherdev, A.V.; Gaur, M.S.; Dzantiev, B.B. Colorimetric Determination of Lead Using Gold Nanoparticles. *Anal. Lett.* **2014**, *48*, 766–782. <https://doi.org/10.1080/00032719.2014.961641>.
46. Yoosaf, K.; Ipe, B.I.; Suresh, C.H.; Thomas, K.G. In Situ Synthesis of Metal Nanoparticles and Selective Naked-Eye Detection of Lead Ions from Aqueous Media. *J. Phys. Chem. C* **2007**, *111*, 12839–12847.

47. Sau, T.K.; Murphy, C.J. Seeded High Yield Synthesis of Short Au Nanorods in Aqueous Solution. *Langmuir* **2004**, *20*, 6414–6420.
48. Ye, X.; Jin, L.; Caglayan, H.; Chen, J.; Xing, G.; Zheng, C.; Doan-Nguyen, V.; Kang, Y.; Engheta, N.; Kagan, C.R.; et al. Improved Size-Tunable Synthesis of Monodisperse Gold Nanorods through the Use of Aromatic Additives. *ACS Nano* **2012**, *6*, 2804–2817.
49. Tan, M.G.; Zhang, G.L.; Li, X.L.; Zhang, Y.X.; Yue, W.S.; Chen, J.M.; Wang, Y.S.; Li, A.G.; Li, Y.; Zhang, Y.M.; et al. Comprehensive Study of Lead Pollution in Shanghai by Multiple Techniques. *Anal. Chem.* **2006**, *78*, 8044–8050.
50. Raj, K.; Das, A.P. Lead pollution: Impact on environment and human health and approach for a sustainable solution. *Environ. Chem. Ecotox* **2023**, *5*, 79–85. <https://doi.org/10.1016/j.enceco.2023.02.001>.
51. Collin, M.S.; Venkatraman, S.K.; Vijayakumar, N.; Kanimozhi, V.; Arbaaz, S.M.; Stacey, R.G.S.; Anusha, J.; Choudhary, R.; Lvov, V.; Tovar, G.I.; et al. Bioaccumulation of lead (Pb) and its effects on human: A review. *J. Hazard. Mater. Adv.* **2022**, *7*, 100094. <https://doi.org/10.1016/j.hazadv.2022.100094>.
52. Reuben, A.; Caspi, A.; Belsky, D.W.; Broadbent, J.; Harrington, H.; Sugden, K.; Houts, R.M.; Ramrakha, S.; Poulton, R.; Moffitt, T.E. Association of Childhood Blood Lead Levels With Cognitive Function and Socioeconomic Status at Age 38 Years and With IQ Change and Socioeconomic Mobility Between Childhood and Adulthood. *JAMA* **2017**, *317*, 1244–1251. <https://doi.org/10.1001/jama.2017.1712>.
53. Frost, M.S.; Dempsey, M.J.; Whitehead, D.E. The response of citrate functionalised gold and silver nanoparticles to the addition of heavy metal ions. *Colloids Surf. A* **2017**, *518*, 15–24. <https://doi.org/10.1016/j.colsurfa.2016.12.036>.
54. Huang, K.W.; Yu, C.J.; Tseng, W.L. Sensitivity enhancement in the colorimetric detection of lead(II) ion using gallic acid-capped gold nanoparticles: Improving size distribution and minimizing interparticle repulsion. *Biosens. Bioelectron.* **2010**, *25*, 984–989. <https://doi.org/10.1016/j.bios.2009.09.006>.
55. Lee, I.L.; Sung, Y.-M.; Wu, S.-P. Triazole-acetate functionalized gold nanoparticles for colorimetric Pb(ii) sensing. *RSC Adv.* **2014**, *4*, 25251–25256. <https://doi.org/10.1039/c4ra02448f>.
56. Khanna, K.; Kohli, S.K.; Kumar, P.; Ohri, P.; Bhardwaj, R.; Alam, P.; Ahmad, P. Arsenic as hazardous pollutant: Perspectives on engineering remediation tools. *Sci. Total Environ.* **2022**, *838*, 155870. <https://doi.org/10.1016/j.scitotenv.2022.155870>.
57. Hughes, M.F. Arsenic toxicity and potential mechanisms of action. *Toxicol. Lett.* **2002**, *133*, 1–16.
58. Gong, L.; Du, B.; Pan, L.; Liu, Q.; Yang, K.; Wang, W.; Zhao, H.; Wu, L.; He, Y. Colorimetric aggregation assay for arsenic(III) using gold nanoparticles. *Microchim. Acta* **2017**, *184*, 1185–1190. <https://doi.org/10.1007/s00604-017-2122-6>.
59. Boruah, B.S.; Biswas, R.; Deb, P. A green colorimetric approach towards detection of arsenic (III): A pervasive environmental pollutant. *Opt. Laser Technol.* **2019**, *111*, 825–829. <https://doi.org/10.1016/j.optlastec.2018.09.023>.
60. Hylander, L.D.; Goodsite, M.E. Environmental costs of mercury pollution. *Sci. Total Environ.* **2006**, *368*, 352–370. <https://doi.org/10.1016/j.scitotenv.2005.11.029>.
61. Bernhoft, R.A. Mercury toxicity and treatment: A review of the literature. *J. Environ. Public Health* **2012**, *2012*, 460508. <https://doi.org/10.1155/2012/460508>.
62. Zhu, Y.; Cai, Y.; Zhu, Y.; Zheng, L.; Ding, J.; Quan, Y.; Wang, L.; Qi, B. Highly sensitive colorimetric sensor for Hg²⁺ detection based on cationic polymer/DNA interaction. *Biosens. Bioelectron.* **2015**, *69*, 174–178. <https://doi.org/10.1016/j.bios.2015.02.018>.
63. Chen, L.; Li, J.; Chen, L. Colorimetric detection of mercury species based on functionalized gold nanoparticles. *ACS Appl. Mater. Interfaces* **2014**, *6*, 15897–15904. <https://doi.org/10.1021/am503531c>.
64. Hu, Y.; Huang, Z.; Liu, B.; Liu, J. Hg(II) Adsorption on Gold Nanoparticles Dominates DNA-Based Label-Free Colorimetric Sensing. *ACS Appl. Nano Mater.* **2021**, *4*, 1377–1384. <https://doi.org/10.1021/acsanm.0c02923>.
65. Alasfar, R.H.; Isaifan, R.J. Aluminum environmental pollution: The silent killer. *Environ. Sci. Pollut. Res.* **2021**, *28*, 44587–44597. <https://doi.org/10.1007/s11356-021-14700-0>.
66. Bonfiglio, R.; Scimeca, M.; Mauriello, A. The impact of aluminum exposure on human health. *Arch. Toxicol.* **2023**, *97*, 2997–2998. <https://doi.org/10.1007/s00204-023-03581-6>.
67. Luo, X.; Xie, X.; Meng, Y.; Sun, T.; Ding, J.; Zhou, W. Ligands dissociation induced gold nanoparticles aggregation for colorimetric Al³⁺ detection. *Anal. Chim. Acta* **2019**, *1087*, 76–85. <https://doi.org/10.1016/j.aca.2019.08.045>.
68. Megarajan, S.; Veerappan, A. A selective pink-to-purple colorimetric sensor for aluminium via the aggregation of gold nanoparticles. *Opt. Mater.* **2020**, *108*, 110177. <https://doi.org/10.1016/j.optmat.2020.110177>.
69. Huang, P.; Li, J.; Liu, X.; Wu, F. Colorimetric determination of aluminum(III) based on the aggregation of Schiff base-functionalized gold nanoparticles. *Microchim. Acta* **2015**, *183*, 863–869. <https://doi.org/10.1007/s00604-015-1734-y>.
70. Li, X.; Xu, G.; Xia, M.; Liu, X.; Fan, F.; Dou, J. Research on the remediation of cesium pollution by adsorption: Insights from bibliometric analysis. *Chemosphere* **2022**, *308*, 136445. <https://doi.org/10.1016/j.chemosphere.2022.136445>.

71. Qiu, J.; Fu, L.; Wang, H.; Zou, R.; Zhang, Y.; Li, X.; Wu, A. Colorimetric detection of Cs⁺ based on the nonmorphological transition mechanism of gold nanoparticles in the presence of Prussian blue. *New J. Chem.* **2020**, *44*, 2241–2246. <https://doi.org/10.1039/c9nj05301h>.
72. Tsepina, N.; Kolesnikov, S.; Minnikova, T.; Timoshenko, A.; Kazeev, K. Soil Contamination by Silver and Assessment of Its Ecotoxicity. *Rev. Agric. Sci.* **2022**, *10*, 186–205. https://doi.org/10.7831/ras.10.0_186.
73. Wang, F.; Lu, Y.; Chen, Y.; Sun, J.; Liu, Y. Colorimetric Nanosensor Based on the Aggregation of AuNP Triggered by Carbon Quantum Dots for Detection of Ag⁺ Ions. *ACS Sustain. Chem. Eng* **2018**, *6*, 3706–3713. <https://doi.org/10.1021/acssuschemeng.7b04067>.
74. Peter, A.L.; Viraraghavan, T. Thallium: A review of public health and environmental concerns. *Environ. Int* **2005**, *31*, 493–501. <https://doi.org/10.1016/j.envint.2004.09.003>.
75. Lei, F.; Ye, Z.; Dong, Z.; Zhang, X.; Wu, P. Thioflavine T-induced charge neutralization assembly of AuNPs for colorimetric sensing of thallium. *Sens. Actuators B Chem.* **2022**, *370*, 132437. <https://doi.org/10.1016/j.snb.2022.132437>.
76. Botelho Junior, A.B.; Espinosa, D.C.R.; Vaughan, J.; Tenório, J.A.S. Recovery of scandium from various sources: A critical review of the state of the art and future prospects. *Miner. Eng.* **2021**, *172*, 107148. <https://doi.org/10.1016/j.mineng.2021.107148>.
77. Tanida, E.; Usuda, K.; Kono, K.; Kawano, A.; Tsuji, H.; Imanishi, M.; Suzuki, S.; Ohnishi, K.; Yamamoto, K. Urinary scandium as predictor of exposure: Effects of scandium chloride hexahydrate on renal function in rats. *Biol. Trace Elem. Res.* **2009**, *130*, 273–282. <https://doi.org/10.1007/s12011-009-8337-6>.
78. Deng, H.-H.; Huang, K.-Y.; Fang, Q.-H.; Lv, Y.-P.; He, S.-B.; Peng, H.-P.; Xia, X.-H.; Chen, W. Schiff base and Lewis acid-base interaction-regulated aggregation/dispersion of gold nanoparticles for colorimetric recognition of rare-earth Sc³⁺ ions. *Sens. Actuators B Chem.* **2020**, *311*, 127925. <https://doi.org/10.1016/j.snb.2020.127925>.
79. Barber, T.R.; Lutes, C.C.; Doorn, M.R.J.; Fuchsman, P.C.; Timmenga, H.J.; Crouch, R.L. Aquatic ecological risks due to cyanide releases from biomass burning. *Chemosphere* **2003**, *50*, 343–348.
80. Jaszczak, E.; Polkowska, Z.; Narkowicz, S.; Namiesnik, J. Cyanides in the environment-analysis-problems and challenges. *Environ. Sci. Pollut. Res.* **2017**, *24*, 15929–15948. <https://doi.org/10.1007/s11356-017-9081-7>.
81. Cheng, C.; Chen, H.-Y.; Wu, C.-S.; Meena, J.S.; Simon, T.; Ko, F.-H. A highly sensitive and selective cyanide detection using a gold nanoparticle-based dual fluorescence–colorimetric sensor with a wide concentration range. *Sens. Actuators B Chem.* **2016**, *227*, 283–290. <https://doi.org/10.1016/j.snb.2015.12.057>.
82. Camargo, J.A.; Alonso, A. Ecological and toxicological effects of inorganic nitrogen pollution in aquatic ecosystems: A global assessment. *Environ. Int* **2006**, *32*, 831–849. <https://doi.org/10.1016/j.envint.2006.05.002>.
83. Picetti, R.; Deeney, M.; Pastorino, S.; Miller, M.R.; Shah, A.; Leon, D.A.; Dangour, A.D.; Green, R. Nitrate and nitrite contamination in drinking water and cancer risk: A systematic review with meta-analysis. *Environ. Res.* **2022**, *210*, 112988. <https://doi.org/10.1016/j.envres.2022.112988>.
84. Sener, G.; Uzun, L.; Denizli, A. Colorimetric sensor array based on gold nanoparticles and amino acids for identification of toxic metal ions in water. *ACS Appl. Mater. Interfaces* **2014**, *6*, 18395–18400. <https://doi.org/10.1021/am5071283>.
85. Li, X.; Li, S.; Liu, Q.; Chen, Z. Electronic-Tongue Colorimetric-Sensor Array for Discrimination and Quantitation of Metal Ions Based on Gold-Nanoparticle Aggregation. *Anal. Chem.* **2019**, *91*, 6315–6320. <https://doi.org/10.1021/acs.analchem.9b01139>.
86. Qiu, J.; Li, Z.; Miao, L.; Wang, H.; Zhang, Y.; Wu, S.; Zhang, Y.; Li, X.; Wu, A. Colorimetric detection of Ba²⁺, Cd²⁺ and Pb²⁺ based on a multifunctionalized Au NP sensor. *Analyst* **2019**, *144*, 5081–5089. <https://doi.org/10.1039/c9an00836e>.
87. Guo, Y.; Wang, Z.; Qu, W.; Shao, H.; Jiang, X. Colorimetric detection of mercury, lead and copper ions simultaneously using protein-functionalized gold nanoparticles. *Biosens. Bioelectron.* **2011**, *26*, 4064–4069. <https://doi.org/10.1016/j.bios.2011.03.033>.
88. Zhang, W.; Jiang, F.; Ou, J. Global pesticide consumption and pollution: With China as a focus. *Proc. Int. Acad. Ecol. Environ. Sci.* **2011**, *1*, 125–144.
89. Jeyaseelan, A.; Murugesan, K.; Thayanthi, S.; Palanisamy, S.B. A review of the impact of herbicides and insecticides on the microbial communities. *Environ. Res.* **2024**, *245*, 118020. <https://doi.org/10.1016/j.envres.2023.118020>.
90. Kim, K.H.; Kabir, E.; Jahan, S.A. Exposure to pesticides and the associated human health effects. *Sci Total Environ.* **2017**, *575*, 525–535. <https://doi.org/10.1016/j.scitotenv.2016.09.009>.
91. Fahimi-Kashani, N.; Hormozi-Nezhad, M.R. Gold-Nanoparticle-Based Colorimetric Sensor Array for Discrimination of Organophosphate Pesticides. *Anal. Chem.* **2016**, *88*, 8099–8106. <https://doi.org/10.1021/acs.analchem.6b01616>.
92. Chen, N.; Liu, H.; Zhang, Y.; Zhou, Z.; Fan, W.; Yu, G.; Shen, Z.; Wu, A. A colorimetric sensor based on citrate-stabilized AuNPs for rapid pesticide residue detection of terbuthylazine and dimethoate. *Sens. Actuators B Chem.* **2018**, *255*, 3093–3101. <https://doi.org/10.1016/j.snb.2017.09.134>.

93. Zhou, Y.; Li, C.; Liu, R.; Chen, Z.; Li, L.; Li, W.; He, Y.; Yuan, L. Label-Free Colorimetric Detection of Prothioconazole Using Gold Nanoparticles Based on One-Step Reaction. *ACS Biomater. Sci. Eng.* **2020**, 6, 2805–2811. <https://doi.org/10.1021/acsbiomaterials.0c00208>.
94. Liu, K.; Jin, Y.; Wu, Y.; Liang, J. Simple and rapid colorimetric visualization of tetramethylthiuram disulfide (thiram) sensing based on anti-aggregation of gold nanoparticles. *Food Chem.* **2022**, 384, 132223. <https://doi.org/10.1016/j.foodchem.2022.132223>.
95. Barbosa, J.; Cruz, C.; Martins, J.; Silva, J.M.; Neves, C.; Alves, C.; Ramos, F.; Da Silveira, M.I. Food poisoning by clenbuterol in Portugal. *Food Addit. Contam.* **2005**, 22, 563–566. <https://doi.org/10.1080/02652030500135102>.
96. Kumari, S.; Pal, B.; Sahu, S.K.; Prabhakar, P.K.; Tewari, D. Adverse events of clenbuterol among athletes: A systematic review of case reports and case series. *Int. J. Leg. Med.* **2023**, 137, 1023–1037. <https://doi.org/10.1007/s00414-023-02996-1>.
97. Kang, J.; Zhang, Y.; Li, X.; Miao, L.; Wu, A. A Rapid Colorimetric Sensor of Clenbuterol Based on Cysteamine-Modified Gold Nanoparticles. *ACS Appl. Mater. Interfaces* **2016**, 8, 1–5. <https://doi.org/10.1021/acsami.5b09079>.
98. Martinez, J.L. Environmental pollution by antibiotics and by antibiotic resistance determinants. *Environ. Pollut.* **2009**, 157, 2893–2902. <https://doi.org/10.1016/j.envpol.2009.05.051>.
99. Polianciuc, S.I.; Gurzau, A.E.; Kiss, B.; Stefan, M.G.; Loghin, F. Antibiotics in the environment: Causes and consequences. *Med. Pharm. Rep.* **2020**, 93, 231–240. <https://doi.org/10.15386/mpr-1742>.
100. Gothwal, R.; Shashidhar, T. Antibiotic Pollution in the Environment: A Review. *CLEAN-Soil Air Water* **2014**, 43, 479–489. <https://doi.org/10.1002/clen.201300989>.
101. Qin, L.; Zeng, G.; Lai, C.; Huang, D.; Zhang, C.; Xu, P.; Hu, T.; Liu, X.; Cheng, M.; Liu, Y.; et al. A visual application of gold nanoparticles: Simple, reliable and sensitive detection of kanamycin based on hydrogen-bonding recognition. *Sens. Actuators B Chem.* **2017**, 243, 946–954. <https://doi.org/10.1016/j.snb.2016.12.086>.
102. Wu, Y.Y.; Huang, P.; Wu, F.Y. A label-free colorimetric aptasensor based on controllable aggregation of AuNPs for the detection of multiplex antibiotics. *Food Chem.* **2020**, 304, 125377. <https://doi.org/10.1016/j.foodchem.2019.125377>.
103. Zhang, S.; Du, X.; Liu, H.; Losiewicz, M.D.; Chen, X.; Ma, Y.; Wang, R.; Tian, Z.; Shi, L.; Guo, H.; et al. The latest advances in the reproductive toxicity of microcystin-LR. *Environ. Res.* **2021**, 192, 110254. <https://doi.org/10.1016/j.envres.2020.110254>.
104. Li, Y.; Wang, Z.; Beier, R.C.; Shen, J.; De Smet, D.; De Saeger, S.; Zhang, S. T-2 toxin, a trichothecene mycotoxin: Review of toxicity, metabolism, and analytical methods. *J. Agric. Food Chem.* **2011**, 59, 3441–3453. <https://doi.org/10.1021/jf200767q>.
105. Rochester, J.R. Bisphenol A and human health: A review of the literature. *Reprod. Toxicol.* **2013**, 42, 132–155. <https://doi.org/10.1016/j.reprotox.2013.08.008>.
106. Li, X.; Cheng, R.; Shi, H.; Tang, B.; Xiao, H.; Zhao, G. A simple highly sensitive and selective aptamer-based colorimetric sensor for environmental toxins microcystin-LR in water samples. *J. Hazard. Mater.* **2016**, 304, 474–480. <https://doi.org/10.1016/j.jhazmat.2015.11.016>.
107. Zhang, W.; Wang, Y.; Nan, M.; Li, Y.; Yun, J.; Wang, Y.; Bi, Y. Novel colorimetric aptasensor based on unmodified gold nanoparticle and ssDNA for rapid and sensitive detection of T-2 toxin. *Food Chem.* **2021**, 348, 129128. <https://doi.org/10.1016/j.foodchem.2021.129128>.
108. Lee, E.H.; Lee, S.K.; Kim, M.J.; Lee, S.W. Simple and rapid detection of bisphenol A using a gold nanoparticle-based colorimetric aptasensor. *Food Chem.* **2019**, 287, 205–213. <https://doi.org/10.1016/j.foodchem.2019.02.079>.
109. Becalski, A.; Lau, B.P.-Y.; Lewis, D.; Seaman, S.W. Semicarbazide Formation in Azodicarbonamide-Treated Flour: A Model Study. *J. Agric. Food Chem.* **2004**, 52, 5730–5734.
110. Chen, Z.; Chen, L.; Lin, L.; Wu, Y.; Fu, F. A Colorimetric Sensor for the Visual Detection of Azodicarbonamide in Flour Based on Azodicarbonamide-Induced Anti-Aggregation of Gold Nanoparticles. *ACS Sens.* **2018**, 3, 2145–2151. <https://doi.org/10.1021/acssensors.8b00705>.
111. Bourdin, D.; Mocho, P.; Desauziers, V.; Plaisance, H. Formaldehyde emission behavior of building materials: On-site measurements and modeling approach to predict indoor air pollution. *J. Hazard. Mater.* **2014**, 280, 164–173. <https://doi.org/10.1016/j.jhazmat.2014.07.065>.
112. Tang, X.; Bai, Y.; Duong, A.; Smith, M.T.; Li, L.; Zhang, L. Formaldehyde in China: Production, consumption, exposure levels, and health effects. *Environ. Int.* **2009**, 35, 1210–1224. <https://doi.org/10.1016/j.envint.2009.06.002>.
113. Almaquer, F.E.P.; Ricacho, J.S.Y.; Ronquillo, R.L.G. Simple and rapid colorimetric sensing of Ni(II) ions in tap water based on aggregation of citrate-stabilized silver nanoparticles. *Sustain. Environ. Res.* **2019**, 29, 23. <https://doi.org/10.1186/s42834-019-0026-3>.
114. Li, H.; Cui, Z.; Han, C. Glutathione-stabilized silver nanoparticles as colorimetric sensor for Ni²⁺ ion. *Sens. Actuators B Chem.* **2009**, 143, 87–92. <https://doi.org/10.1016/j.snb.2009.09.013>.
115. Karthiga, D.; Anthony, S.P. Selective colorimetric sensing of toxic metal cations by green synthesized silver nanoparticles over a wide pH range. *RSC Adv.* **2013**, 3, 16765–16774. <https://doi.org/10.1039/c3ra42308e>.

116. Soomro, R.A.; Nafady, A.; Sirajuddin; Memon, N.; Sherazi, T.H.; Kalwar, N.H. L-cysteine protected copper nanoparticles as colorimetric sensor for mercuric ions. *Talanta* **2014**, *130*, 415–422. <https://doi.org/10.1016/j.talanta.2014.07.023>.
117. Li, Q.; Wu, F.; Mao, M.; Ji, X.; Wei, L.; Li, J.; Ma, L. A dual-mode colorimetric sensor based on copper nanoparticles for the detection of mercury-(ii) ions. *Anal. Methods* **2019**, *11*, 4014–4021. <https://doi.org/10.1039/c9ay00843h>.
118. Madhupriya, S.; Elango, K.P. Highly selective colorimetric sensing of Cu(II) ions in aqueous solution via modulation of intramolecular charge transfer transition of aminonaphthoquinone chemosensor. *Spectrochim Acta A Mol Biomol Spectrosc* **2012**, *97*, 100–104. <https://doi.org/10.1016/j.saa.2012.05.044>.
119. Petdum, A.; Panchan, W.; Sirirak, J.; Promarak, V.; Sooksimuang, T.; Wanichacheva, N. Colorimetric and fluorescent sensing of a new FRET system via [5]helicene and rhodamine 6G for Hg²⁺ detection. *New J. Chem.* **2018**, *42*, 1396–1402. <https://doi.org/10.1039/c7nj04129b>.
120. Chen, L.; Tian, X.; Xia, D.; Nie, Y.; Lu, L.; Yang, C.; Zhou, Z. Novel Colorimetric Method for Simultaneous Detection and Identification of Multimetal Ions in Water: Sensitivity, Selectivity, and Recognition Mechanism. *ACS Omega* **2019**, *4*, 5915–5922. <https://doi.org/10.1021/acsomega.9b00312>.
121. Lu, F.; Zhou, Y.-h.; Wu, L.-h.; Qian, J.; Cao, S.; Deng, Y.-f.; Chen, Y. Highly Fluorescent Nitrogen-Doped Graphene Quantum Dots' Synthesis and Their Applications as Fe(III) Ions Sensor. *Int. J. Opt.* **2019**, *2019*, 8724320. <https://doi.org/10.1155/2019/8724320>.
122. Li, F.; Hong, Y.-S.; Zuo, K.-X.; Sun, Q.; Gao, E.-Q. Highly selective fluorescent probe for Hg²⁺ and MnO₄⁻ by the two-fold interpenetrating metal-organic framework with nitro functionalized linkers. *J. Solid State Chem.* **2019**, *270*, 509–515. <https://doi.org/10.1016/j.jssc.2018.12.025>.